

THÈSE PRÉSENTÉE
POUR OBTENIR LE GRADE DE
DOCTEUR
DE L'UNIVERSITÉ DE BORDEAUX
ECOLE DOCTORALE SCIENCES PHYSIQUES ET DE
L'INGÉNIEUR
LASERS, MATIÈRE, NANOSCIENCES

Par **Maxime Lavaud**

Confined Brownian Motion

Sous la direction de : **Thomas Salez**
Co-directrion : **Yacine Amarouchene**

Soutenue le 25 décembre 2019

Membres du jury :

Mme. Aude ALPHA	Directrice de Recherche	Université	Rapporteur
M. Bernard BETA	Directeur de Recherche	Université	Rapporteur
M. Georges GAMMA	Directeur de Recherche	Université	Président
Mme. Dominique DELTA	Chargée de Recherche	Université	Examinateuse
M. Eric EPSILON	Ingénieur de Recherche	Université	Examinateur
Mme. Jane DOE	Directrice de Recherche	Université	Directrice
Mme. Simone UNTEL	Ingénieure de Recherche	Université	Invitée

Abstract

Lorem ipsum dolor sit amet, consectetuer adipiscing elit. Ut purus elit, vestibulum ut, placerat ac, adipiscing vitae, felis. Curabitur dictum gravida mauris. Nam arcu libero, nonummy eget, consectetuer id, vulputate a, magna. Donec vehicula augue eu neque. Pellentesque habitant morbi tristique senectus et netus et malesuada fames ac turpis egestas. Mauris ut leo. Cras viverra metus rhoncus sem. Nulla et lectus vestibulum urna fringilla ultrices. Phasellus eu tellus sit amet tortor gravida placerat. Integer sapien est, iaculis in, pretium quis, viverra ac, nunc. Praesent eget sem vel leo ultrices bibendum. Aenean faucibus. Morbi dolor nulla, malesuada eu, pulvinar at, mollis ac, nulla. Curabitur auctor semper nulla. Donec varius orci eget risus. Duis nibh mi, congue eu, accumsan eleifend, sagittis quis, diam. Duis eget orci sit amet orci dignissim rutrum.

Table of Contents

Abstract	i
Table of Contents	ii
List of Figures	v
Nomenclature	vi
List of Abbreviations	vi
1 Introduction	1
2 Brownian motion	3
2.1 The Brownian motion discovery	3
2.2 Einstein's Brownian theory	4
2.3 The Langevin Equation	8
2.4 Numerical simulation of bulk Brownian motion	13
2.4.1 The numerical Langevin Equation	13
2.4.2 Simulating Brownian motion using Python	15
2.4.3 Speedup using Cython	18
2.5 Conclusion	19
3 Particle characterization and particle tracking using interference properties	20
3.1 Introduction	20
3.2 Reflection Interference Contrast Microscopy	20
3.3 Lorenz-Mie Fit	23
3.3.1 Hologram dependance on the particule characteristics	26
3.4 Rayleigh-Sommerfeld back-propagation	32
3.4.1 Conclusion	33
3.5 Experimental setup	34
3.6 Hologram fitting strategy	35
3.6.1 How to fasten the process ?	35
3.6.2 Radius and optical index characterization	36
4 infer	38
4.1 The confined Brownian motion	38
References	42

List of Figures

Fig. 1:	Brownian motion of $1 \mu\text{m}$ particles in water tracked by hand by Jean Perrin and his colleagues. The points are spaced in time by 30 seconds and 16 divisions represents $50 \mu\text{m}$.	4
Fig. 2:	Simulation of the bulk Brownian motion of $1 \mu\text{m}$ particles in water. On the top each line represents the trajectory of a Brownian particle over 100 seconds. A total of 100 trajectories or shown. On the bottom, bullets represents the Mean Square Displacement (MSD) computed from the simulated trajectories. The black plain line represents Einstein's theory, which is computed from the square of Eq.2.2.11. 	7
Fig. 3:	Bullets represents the probability density function of w_i , a Gaussian distributed number with a mean value $\langle w_i \rangle$ and a variance $\langle w_i^2 \rangle = \tau$. The plain black line represents a gaussian of zero mean and a τ variance, Eq.2.4.3. On the first line simulation is done with $\tau = 10^{-3} \text{ s}$ and $\tau = 1 \text{ s}$ on the second one. Each column correspond to a number of draw N , from the left to the right $N = 10^2, 10^3$ and 10^4 .	13
Fig. 4:	Mean Relative Squared Error (MRSE) of the PDF measured from a generation of N Gaussian random number w_i , and, the actual Gaussian over which the generation is done, Eq.2.4.3. The generation is done over a Gaussian which has a mean value $\langle w_i \rangle = 0$ and the variance $\langle w_i^2 \rangle = \tau$. We explore generation ranging from $N = 10$ to 10^7 and $\tau = 10^{-2}$ to 10 s	15
Fig. 5:	a) Set of 100 trajectories simulated using the full Langevin equation for particle of a radius $a = 1 \mu\text{m}$ and a mass $m = 10 \mu\text{g}$ in water, $\eta = 0.001 \text{ Pa.s}$. The simulations are done with a time step $\tau = 0.01 \text{ s}$. b) Bullets represents the measured Mean Squared Displacement (MSD) of the simulated trajectories. The plain black line represents the characteristic time of the diffusion, here $\tau_B = m/\gamma = 0.53 \text{ s}$. The dotted line represents the MSD theory when $t \ll \tau_B$, $\text{MSD} = \tau^2 k_B T/m$. The dashed line when $t \gg \tau_B$, $\text{MSD} = 2D\tau$. A detailed explanation of the simulation process can be found in the appendix.??.	18
Fig. 6:	Figure from [38] representing RICM with two wavelengths. (a) Left: interference patterns created with a wavelength $\lambda_1 = 532 \text{ nm}$ (scale bar $5 \mu\text{m}$). Right: radial intensity profile (black dots) extracted from the image, azimuthally averaged (magenta line) and fitted with Eq.3.2.8 to measure the height of the particle (here h). (b) Same as (a) with a wavelength $\lambda_2 = 635 \text{ nm}$. (c) Time series of the height of a particle h (green: λ_1 , magenta: λ_2) and the particle velocity measured along the flow in blue.	21

Fig. 7:	a) Raw hologram of a $2.5 \mu\text{m}$ polystyrene particle measured experimentally with the setup detailed in the chapter 3.5. b) Background obtained by taking the median value of the time series of images of the diffusing particle. c) Normalized hologram given by dividing a) by b). d) Result of the fit of c) using Eq.3.3.4 the particle is found to be at a height $z = 14.77 \mu\text{m}$. e) Comparison of the normalized radial intensity, obtained experimentally from c) and theoretically from d).	26
Fig. 8:	On the left, experimentally measured holograms' radial intensity profile stack, generated from a polystyrene bead of nominal radius $a = 1.5 \pm 0.035 \mu\text{m}$ using the experimental setup explained in chapter 3.5. The calibration of this particle radius and optical index is shown in Fig.17. On the right, the corresponding theoretical stack using the result of each individual hologram's fit.	27
Fig. 9:	On the left, experimentally measured holograms' radial intensity profile stack, generated from a polystyrene bead of nominal radius $a = 1.5 \pm 0.035 \mu\text{m}$ using the experimental setup explained in chapter 3.5. The calibration of this particle radius and optical index is shown in Fig.17. On the right, the corresponding theoretical stack using the result of each individual hologram's fit.	28
Fig. 10:	On the left, experimentally measured holograms' radial intensity profile stack, generated from a polystyrene bead of nominal radius $a = 1.5 \pm 0.035 \mu\text{m}$ using the experimental setup explained in chapter 3.5. The calibration of this particle radius and optical index is shown in Fig.17. On the right, the corresponding theoretical stack using the result of each individual hologram's fit.	28
Fig. 11:	On the left, experimentally measured holograms' radial intensity profile stack, generated from a polystyrene bead of nominal radius $a = 1.5 \pm 0.035 \mu\text{m}$ using the experimental setup explained in chapter 3.5. The calibration of this particle radius and optical index is shown in Fig.17. On the right, the corresponding theoretical stack using the result of each individual hologram's fit.	29
Fig. 12:	On the left, experimentally measured holograms' radial intensity profile stack, generated from a polystyrene bead of nominal radius $a = 1.5 \pm 0.035 \mu\text{m}$ using the experimental setup explained in chapter 3.5. The calibration of this particle radius and optical index is shown in Fig.17. On the right, the corresponding theoretical stack using the result of each individual hologram's fit.	30

Fig. 13:	On the left, experimentally measured holograms' radial intensity profile stack, generated from a polystyrene bead of nominal radius $a = 1.5 \pm 0.035 \mu\text{m}$ using the experimental setup explained in chapter 3.5. The calibration of this particle radius and optical index is shown in Fig.17. On the right, the corresponding theoretical stack using the result of each individual hologram's fit.	31
Fig. 14:	Figure from [65] a) Volumetric reconstruction using Eq.3.4.5 of the scattered intensity of single colloidal sphere, colored by intensity. b) Volumetric reconstructions of 22 individual $1.58 \mu\text{m}$ diameter silica spheres organized in bcc lattice using holographic optical tweezers in distilled water. Colored regions indicate the isosurface of the brightest 1 percent of reconstructed voxels.	33
Fig. 15:	Photo of the custom build microscope used along my thesis. It is mainly composed of Thorlabs cage system. The camera used is a Basler acA1920-155um, we use a x60 magnification and 1.30 numerical aperture oil-immersion objective lens. The light source is a collimated $521 \mu\text{m}$ wavelength laser.	34
Fig. 16:	Schematic of the experimental setup. A laser plane wave of intensity I_0 illuminates the chamber containing a dilute suspension of micro-spheres in water. The light scattered by a particle interferes with the incident beam onto the focal plane of an objective lens, that magnifies the interference pattern and relays it to a camera.	35
Fig. 17:	2D Probability density function of the measurements of the optical index n_p and radius a . Black lines indicate iso-probability. Taking the 10% top probability, we measure $n_p = 1.585 \pm 0.002$ and $a = 1.514 \pm 0.003 \mu\text{m}$	37
Fig. 18:	Figure extracted from [13], on the left is the experimental setup used. It is an inverted microscope used in order to track particle of size $2R$ inside a cell of thickness t . On the right is their final result, where they measure the diffusion parallel coefficient D_\perp given by Eq.4.1.2, here normalized by D_0 the bulk diffusion coefficient as a function of γ a confinement constant $\gamma = (\langle z \rangle - a)/a$	39
Fig. 19:	On the left, plot of the Gibbs-Boltzmann distribution Eq.4.1.10 for $a = 1 \mu\text{m}$, $B = 4$, $\ell_D = 100 \text{ nm}$ and $\Delta\rho = 50 \text{ kg.m}^{-3}$. On the right, local diffusion coefficient normalized by bulk diffusion coefficient $D_0 = k_B T/\gamma$, given by Eq.4.1.2 and Eq.4.1.1	41

List of Abbreviations

fps	Frames per second
MRSE	Mean Relative Squared Error
MSD	Mean Squared Displacement
PDF	Probability Density Function
RICM	Reflection Interference Contrast Microscopy
SDE	Stochastic Differential Equations

1 Introduction

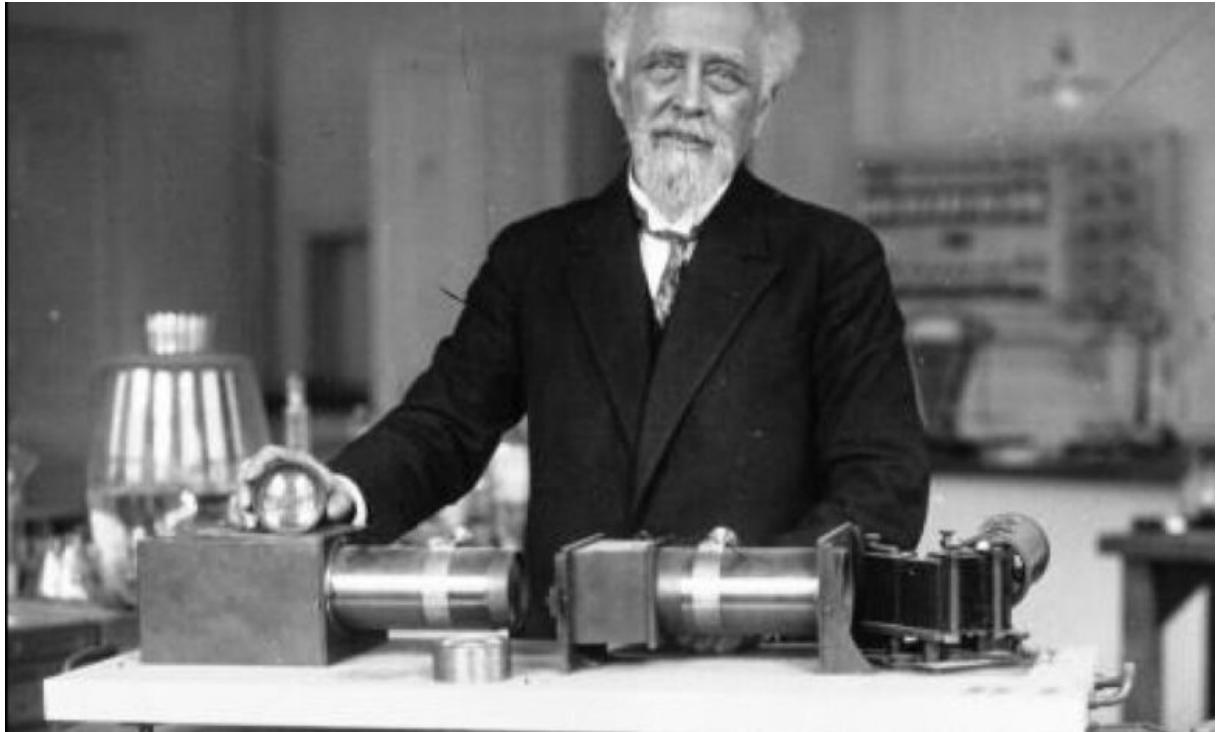
Since the observations of Gordon Moore in the 60's we know that the technological progress is bound to our ability to miniaturize. It's indeed due to the miniaturization that we are able to have more computational power leading to the rise of knew technologies like the Deep Learning [1] that showed the need of large computational capabilities by having the computer program *AlphaGo* beating *Lee Sedol* one of the greatest player of *Go* in 2016. Since this powerful demonstration AIs using the same technologies are showing up in every field, from the language translator to autonomous cars and is know starting to be extensively used in physics with in 2020 the first focus session on machine learning at the *March Meeting* that continued this year with presentations at every sessions. The success of Deep learning is not due to the fact that it's new and fancy algorithm since it known for several decade but only the fact that the miniaturization permitted to do the stunning amount of computation needed to have a smart AI. Our ability to use this technologies is finally bound to our ability to understand the surface physics at the manometer scale.

On another side we have microfluidic since the 80s which is an incredible multidisciplinary field involving chemistry, engineering, soft matter physics and also biotechnology. Microfluidic permitted the development of daily life technologies like the ink-jet printers or more advanced tools such as DNA chips [2] or lab-on-a-chip technology [3]. The ability to compose with a lot of different system to build microfluidic systems is a wonderful playground for physicists which gave a lot of complex systems in confinement to study and understand how different boundaries can change the dynamic properties of a system. At a time of miniaturization and nanotechnologies, the need of tools permitting the systematic study of complex confined system is a key.

In order to address these challenges my work in the past three years focused on using the confined Brownian motion. Brownian Motion is a central paradigm in modern science. It has implications in fundamental physics, biology, and even finance, to name a few. By understanding that the apparent erratic motion of colloids is a direct consequence of the thermal motion of surrounding fluid molecules, pioneers like Einstein and Perrin provided decisive evidence for the existence of atoms [4, 5]. Specifically, free Brownian motion in the bulk us characterized by a typical spatial extent evolving as the square root of time, as well as Gaussian displacements. At a time of miniaturization and interfacial science, and moving beyond the idealized bulk picture, it is relevant to consider the added roles of boundaries to the above context. Indeed, Brownian motion at interfaces and in confinement is a widespread practical situation in microbiology and nanofluidics. In such case, surface effects become dominant and alter drastically the Brownian statistics, with key

implications towards: i) the understanding and smart control of the interfacial dynamics of microscale entities; and ii) high-resolution measurements of surface forces at equilibrium. Interestingly, a confined colloid will exhibit non-Gaussian statistics in displacements, due to the presence of multiplicative noises induced by the hindered mobility near the wall [6–8]. Besides, the particle can be subjected to electrostatic or Van der Waals forces [9] exerted by the interface, and might experience slippage too [10, 11]. Considering the two-body problem, the nearby boundary can also induce some effective interaction [12]. Previous studies have designed novel methods to measure the diffusion coefficient of confined colloids [13–18], or to infer surface forces [19–24].

In the first part of the manuscript I will present the history of the Brownian motion and its basic theory. In a second part I will present particle tracking using Mie holography and our experimental setup. Then the third part will focus on one trajectory analysis in order to infer the surface induced effects on the Brownian motion. In a last chapter I will present more complex inference.



2 Brownian motion

2.1 The Brownian motion discovery

In 1827 the Scottish botanist Robert Brown published an article [25] on his observation on the pollen of *Clarkia pulchella* with a lot of details on his thought processes. His experiments were made to understand the flower reproduction, but, as he was looking through the microscope he observed some minute particles ejected from the pollen grains. At first, he thought the goal of this movement was to test the presence of a male organ. In order to test this theory, he extended his observations to Mosses and *Equiseta*, which were drying for a hundred years. However, the fact that this peculiar movement was still observable made him invalidate his theory. Interestingly each time that he encountered a material that he was able to reduce to a fine enough powder to be suspended in water, he observed the same type of motion, although, he never understood its particle's movement.

The difficulty at this time to observe and capture such a movement made the study of what we call today Brownian motion quite difficult and the first theoretical work was actually done by Louis Bachelier in his PhD thesis “The theory of speculation”, where he described a stochastic analysis of the stock and option market. Nowadays, the mathematical description of random movement is still used in the modern financial industry.

It is finally in 1905 that Albert Einstein theoretically state that “bodies of microscopically visible size suspended in a liquid will perform movements of such a magnitude that they can be easily observed in a microscope” [4]. A remark to make here is that in 1948 Einstein wrote a letter to one of his friend where he stated having deduced the Brownian motion “from mechanics, without knowing that anyone had already observed anything of the kind” [26].

It is in 1908 that Jean Perrin published his experimental work on Brownian motion. that way he was able to measure the Avogadro number and prove the kinetic theory that Einstein developed. I would also cite Chaudesaigues and Dabrowski, who helped Perrin to track the particles by hand, half-minutes by half-minutes, for more than 3000 displacements (25 hours) and several particles. This impressive and daunting work is highly detailed in “*Mouvement brownien et molécules*” [27]. This is partly due the results this work that Perrin received the Nobel award in 1926.

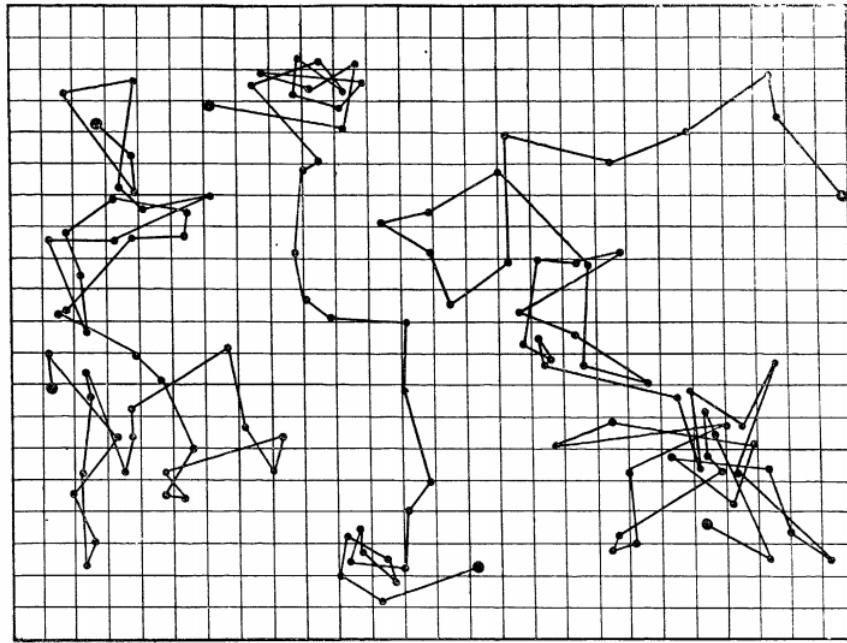


Figure 1: Brownian motion of $1 \mu\text{m}$ particles in water tracked by hand by Jean Perrin and his colleagues. The points are spaced in time by 30 seconds and 16 divisions represents $50 \mu\text{m}$.

2.2 Einstein's Brownian theory

In this section we will derive the main characteristics of bulk Brownian motion in the manner of Einstein in 1905 by summarizing the section 4 of [4]. We will then examine the random motion of particles suspended in a liquid and its relation to diffusion, caused by thermal molecular motion. We assume that each particle motion is independent of other particles; also the motions of one particle at different times are assumed to be independent of one another provided that the time interval is not too small. Furthermore, we now introduce a time interval τ which is small compared to the observation time but large enough so that the displacements in two consecutive time intervals τ may be taken as independent events.

For simplicity, we will here look only at the Brownian motion of n particles in 1D along the x axis. In a time interval τ the position of each individual particle will increase by a displacement Δ , positive or negative. The number of particles dn experiencing a displacement lying between Δ and $\Delta + d\Delta$ in a time interval τ is written as:

$$dn = n\varphi(\Delta)d\Delta , \quad (2.2.1)$$

where

$$\int_{-\infty}^{\infty} \varphi(\Delta) d\Delta = 1 , \quad (2.2.2)$$

and φ is nonzero only for very small displacement Δ and satisfies $\varphi(\Delta) = \varphi(-\Delta)$.

Let $f(x, t)$ be the number of particles per unit volume. From the definition of the function $\varphi(\Delta)$ we can obtain the distribution of particles found at time $t + \tau$ from their distribution at a time t , through:

$$f(x, t + \tau) dx = dx \int_{\Delta=-\infty}^{\Delta=+\infty} f(x + \Delta, t) \varphi(\Delta) d\Delta . \quad (2.2.3)$$

Since τ is very small, we have:

$$f(x, t + \tau) = f(x, t) + \tau \frac{\partial f}{\partial t} . \quad (2.2.4)$$

On the other side we can Taylor expand $f(x + \Delta, t)$ in powers of Δ since only small values of Δ contribute. We obtain:

$$f(x + \Delta, t) = f(x, t) + \Delta \frac{\partial f(x, t)}{\partial x} + \frac{\Delta^2}{2!} \frac{\partial^2 f(x, t)}{\partial x^2} \dots \text{ad inf.} \quad (2.2.5)$$

Putting all together, in Eq.2.2.3 we obtain:

$$f + \frac{\partial f}{\partial t} \tau = f \int_{-\infty}^{+\infty} \varphi(\Delta) d\Delta + \frac{\partial f}{\partial x} \int_{-\infty}^{+\infty} \Delta \varphi(\Delta) d\Delta + \frac{\partial^2 f}{\partial x^2} \int_{-\infty}^{+\infty} \frac{\Delta^2}{2} \varphi(\Delta) d\Delta \dots \quad (2.2.6)$$

On the right-hand side, since $\varphi(x) = \varphi(-x)$ all even terms will vanish, moreover, all the odd terms will be very small compared to the precedent. Taking into account Eq.2.2.2 and invoking the definition:

$$\frac{1}{\tau} \int_{-\infty}^{+\infty} \frac{\Delta^2}{2} \varphi(\Delta) d\Delta = D , \quad (2.2.7)$$

Eq.2.2.6 finally becomes:

$$\frac{\partial f}{\partial t} = D \frac{\partial^2 f}{\partial x^2}. \quad (2.2.8)$$

We can here recognize a partial equation of diffusion with D the diffusion coefficient. We will now initiate the same position $x = 0$ for all the particles at $t = 0$ as in Fig.2. $f(x, t)dx$ denotes the number of particles whose positions have increased between the times 0 and t by a quantity lying between x and $x + dx$ such that we must have:

$$f(x \neq 0, t = 0) = 0 \text{ and } \int_{-\infty}^{+\infty} f(x, t)dx = n. \quad (2.2.9)$$

The solution Eq.2.2.8 is then the Green's function of the heat equation in the bulk:

$$f(x, t) = \frac{1}{\sqrt{4\pi D}} \frac{\exp\left(\frac{-x^2}{4Dt}\right)}{\sqrt{t}}. \quad (2.2.10)$$

From this solution we can see that the mean value of the displacement along the x axis is equal to 0 and the square root of the arithmetic mean of the squares of displacements (that we commonly call the Root Mean Square Displacement (RMSD)) is given by:

$$\lambda_x = \sqrt{\langle \Delta^2 \rangle} = \sqrt{2Dt}. \quad (2.2.11)$$

The mean displacement is thus proportional to the square root of time. This result is generally the first behavior that we check when we study Brownian motion. In 3D, the square root of the MSD will be given by $\lambda_x \sqrt{3}$.

Previously in his article [4], Einstein had found by writing the thermodynamic equilibrium of a suspension of particles that the diffusion coefficient of a particle should read:

$$D = \frac{RT}{N_A} \frac{1}{6\pi\eta a} = \frac{k_B T}{6\pi\eta a}, \quad (2.2.12)$$

with R the gas constant, T the temperature, N_A the Avogadro number, η the fluid viscosity and k_B the Boltzmann constant. Thus, an experimental measurement of D could lead to a measurement of the Avogadro number since:

$$N_A = \frac{t}{\lambda_x^2} \frac{RT}{3\pi\eta a} . \quad (2.2.13)$$

Furthermore, measuring N_A also gives us the mass of atoms and molecules since the mass of a mole is known; as an example the mass of an oxygen atom will be given by $\frac{16}{N_A}$ and the mass a water molecule by $\frac{18}{N_A}$. Finally, Einstein ends up in article [4] by writing “*Let us hope that a researcher will soon succeed in solving the problem posed here, which is of such importance in the theory of heat!*”. I would like here to emphasize the importance of solving this problem at the very beginning of the 20th century. At this time two theories about the fundamental matter components existed, one involving energy and a continuum description in terms of field, and the other one, discrete atoms, especially supported by Boltzmann and his kinetic theory of gases, used by Einstein. Due to a lot of theoretical misunderstandings and experimental error scientist such as Svedberg or Henri thought that Einstein’s theory was false [28] by even suggesting that the statistical properties of Brownian motion were changing with the pH of the solution. It is finally in 1908 that Chaudesaigues and Perrin published all the evidence to prove Einstein’s theory mainly by their ability to create particle emulsions of well controlled radii.

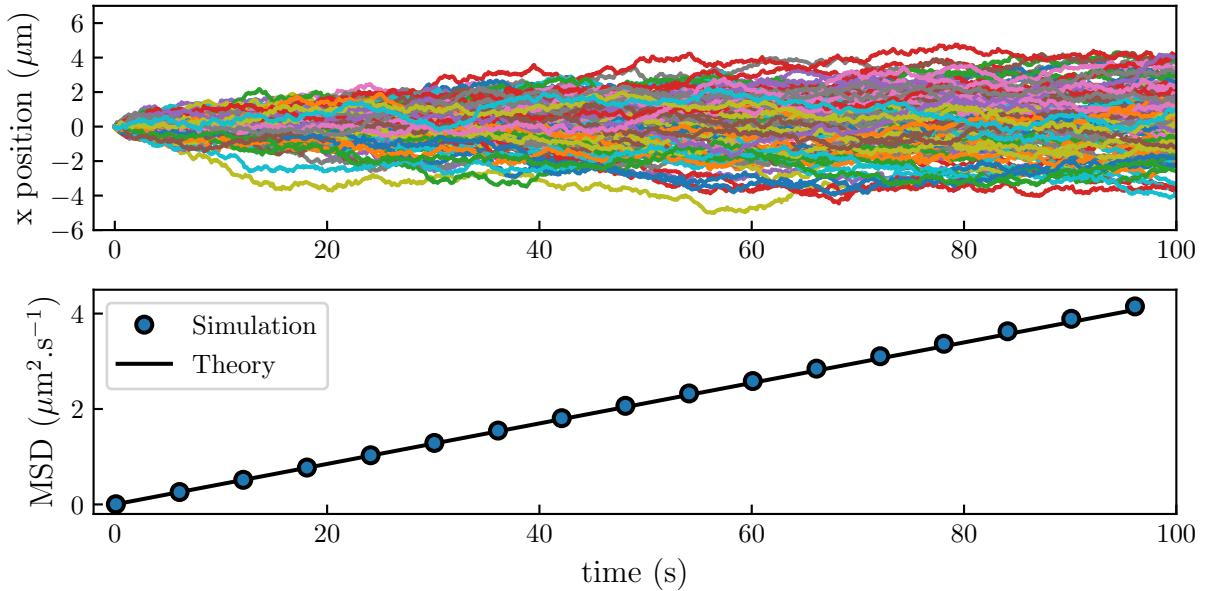


Figure 2: Simulation of the bulk Brownian motion of $1 \mu\text{m}$ particles in water. On the top each line represents the trajectory of a Brownian particle over 100 seconds. A total of 100 trajectories are shown. On the bottom, bullets represent the Mean Square Displacement (MSD) computed from the simulated trajectories. The black plain line represents Einstein’s theory, which is computed from the square of Eq.2.2.11. \clubsuit

2.3 The Langevin Equation

In physics we generally describe Brownian motion through a particular Stochastic Differential Equations (SDE). This model was introduced in 1908 by Langevin [29], this model is now used by the major part of physicists working on random processes. The Langevin equation for a free colloid reads:

$$m dV_t = -\gamma V_t dt + \alpha dB_t , \quad (2.3.1)$$

with m the mass and V_t the velocity of the particle. This SDE is the Newton's second law, relating the particle momentum change on the left-hand side of the equation to forces on the right-hand side. We see that the total force applied on the particle is given by two terms: a friction term, with a Stokes-like fluid friction coefficient γ , a random force with α that we will detail for a spherical particle, dB_t a random noise which has a Gaussian distribution of zero mean thus:

$$\langle dB_t \rangle = 0 , \quad (2.3.2)$$

and variance equal to:

$$\langle dB_t^2 \rangle = dt . \quad (2.3.3)$$

For a spherical particle the friction term is given by the Stoke's formula: $\gamma = 6\pi\eta a$ with η the fluid viscosity and a the particle radius. Thus, we can derive the mean value of the particle velocity as:

$$\langle \frac{dV_t}{dt} \rangle = -\frac{\gamma}{m} \langle V_t \rangle dt + \frac{\alpha}{m} \langle dB_t \rangle , \quad (2.3.4)$$

with the properties of dB_t given by Eq.2.3.2, it becomes:

$$\langle dV_t \rangle = -\frac{\gamma}{m} \langle V_t \rangle dt . \quad (2.3.5)$$

Moreover, without a loss of generality, the average of a variable x , $\langle x \rangle$, is done over a set

of N observations $\{x_i\}$ such as:

$$\langle x \rangle = \frac{1}{N} \sum_{i=1}^N x_i , \quad (2.3.6)$$

one can then show that:

$$\frac{d}{dt} \langle x \rangle = \frac{d}{dt} \left[\frac{1}{N} \sum_{i=1}^N x_i \right] = \frac{1}{N} \sum_{i=1}^N \frac{d}{dt} x_i = \langle \frac{d}{dt} x \rangle . \quad (2.3.7)$$

The latter thus shows that it is possible to invert average value $\langle \cdot \rangle$ and a derivative. Therefor, Eq.2.3.5 becomes:

$$\frac{d}{dt} \langle V_t \rangle = -\frac{\gamma}{m} \langle V_t \rangle , \quad (2.3.8)$$

which has a familiar solution:

$$\langle V_t(t) \rangle = V_0 e^{-\frac{\gamma}{m} t} , \quad (2.3.9)$$

with V_0 an initial velocity. This result shows that the average of the velocity should decay to zero with a characteristic time $\tau_B = \frac{m}{\gamma}$. For instance, the polystyrene particles used during my experiments which are micro-metric we have $\tau_B \approx 10^{-7}$ s. This means that if we measure the displacements of a particle with a time interval $\tau \gg \tau_B$ the displacement can be taken as independent events as it was stated by Einstein. In physical terms, this means that we are in the over-damped regime, in this case the Langevin equation reads:

$$-\gamma V_t dt + \alpha dB_t = 0 . \quad (2.3.10)$$

The experiments done during my thesis used a video camera that can reach a maximum of hundreds frames per second (fps) reaching time steps of $\approx 10^{-2}$ s. Therefore, all my work falls into the over damped regime. Before focusing definitely on Eq.2.3.10, we can use Eq.2.3.4 to characterize further the unknown coefficient α . In order to do so we compute the mean square value of Eq.2.3.4, starting by taking the second order Taylor expansion:

$$\begin{aligned} d(V_t^2) &\simeq \frac{\partial V_t^2}{\partial V_t} dV_t + \frac{1}{2} \frac{\partial^2 V_t^2}{\partial V_t^2} (dV_t)^2 \\ &= 2V_t dV_t + (dV_t)^2 \end{aligned} \quad (2.3.11)$$

combining Eqs.2.3.1 and 2.3.11, we obtain by only keeping the terms of order dt :

$$d(V_t^2) = 2V_t \left(-\frac{\gamma}{m} V_t dt + \frac{\alpha}{m} dB_t \right) + \frac{\alpha^2}{m^2} dB_t^2 . \quad (2.3.12)$$

Thus, the average value of $d(V_t^2)$ reads:

$$\langle d(V_t^2) \rangle = -2\frac{\gamma}{m} \langle V_t^2 \rangle dt + 2\frac{\alpha}{m} \langle V_t dB_t \rangle + \frac{\alpha^2}{m^2} \langle dB_t^2 \rangle . \quad (2.3.13)$$

Moreover, since dB_t is chosen independently of the velocity V_t , one can write $\langle V_t dB_t \rangle = \langle V_t \rangle \langle dB_t \rangle = 0$. Taking the latter remark into account and the fact that $\langle dB_t^2 \rangle = dt$, Eq.2.3.13 becomes:

$$\langle d(V_t^2) \rangle = \left[-2\frac{\gamma}{m} \langle V_t^2 \rangle + \frac{\alpha^2}{m^2} \right] dt . \quad (2.3.14)$$

Since equilibrium averages in thermodynamics must become time independent, we have $\langle d(V_t^2) \rangle = 0$, thus:

$$\langle V_t^2 \rangle = \frac{\alpha^2}{2\gamma m} . \quad (2.3.15)$$

Besides, from the equipartition of energy we also know that:

$$\langle \frac{1}{2} m V_t^2 \rangle = \frac{1}{2} k_B T . \quad (2.3.16)$$

The latter equation permits a direct determination of the amplitude of the noise α :

$$\alpha = \sqrt{2k_B T \gamma} . \quad (2.3.17)$$

The latter result permits to compute the amplitude of the random force in the Langevin equation. Taking the over-damped Langevin equation, it reads:

$$V_t dt = \sqrt{2 \frac{k_B T}{\gamma}} dB_t \quad (2.3.18)$$

Furthermore, one can write the position of the particule X_t at a time t , such as:

$$X_t = \int_0^t V_{t'} dt' , \quad (2.3.19)$$

where we can suppose at the initial time $t = 0$ that $X_0 = 0$. Computing $\langle X_t^2 \rangle$ using Eqs.2.3.18,2.3.19 and 2.3.3 thus gives:

$$\langle X_t^2 \rangle = 2 \frac{k_B T}{\gamma} t = 2 D t \quad (2.3.20)$$

By relating $\langle X_t^2 \rangle$ to the Mean Square Displacement (MSD) to the initial position such as:

$$\text{MSD} = \langle (X_0 - X_t)^2 \rangle = \langle X_t^2 \rangle , \quad (2.3.21)$$

we obtain that the MSD should be linear with the time. This result confirms that using the over-damped Langevin equation, leads to the Einstein's result Eq.2.2.11. Where one can identify the diffusion coefficient of the particle to be $D = k_B T / \gamma$. Additionally, the latter identity is called the Stokes-Einstein relation.

Additionally, the Langevin equation is great to compute correlator such as the velocity correlator $\langle V_t V_{t''} \rangle$ which the simplest to compute and the one that we will detail below. Indeed, if we use the full Langevin equation, $\langle X_t^2 \rangle$ can't be that easily computed since $m dV_t$ does not vanish. We would thus need to rewrite Eq.2.3.20 using the velocity correletor such as:

$$\langle X_t^2 \rangle = \int_0^t \int_0^t \langle V_{t'} V_{t''} \rangle dt' dt'' . \quad (2.3.22)$$

Let us now study how the two-point correlator function $\langle V_t V_{t''} \rangle$, using the full Langevin

equation multiplied by V_0 and following the same steps as for Eq.2.3.9, one has:

$$\langle V_t V_0 \rangle = \langle V_0^2 \rangle e^{-t/\tau_B} . \quad (2.3.23)$$

As the equilibrium state is invariant under temporal translation and assuming that V_0 has an equilibrium steady-state distribution with $\langle V_0^2 \rangle = k_B T / m$ we have:

$$\langle V_t V'_t \rangle = \frac{k_B T}{m} e^{-|t-t'|/\tau_B} . \quad (2.3.24)$$

One can solve Eq.2.3.22 by splitting the integral in two parts, where $t' > t''$ and $t' < t''$:

$$\begin{aligned} \langle X_t^2 \rangle &= \frac{k_B T}{m} \int_0^t dt' \int_0^{t'} dt'' e^{-|t'-t''|/\tau_B} = 2 \frac{k_B T}{\gamma} \left(\int_0^t dt' \left[1 - e^{-t'/\tau_B} \right] \right) \\ &= 2 \frac{k_B T}{\gamma} \left(t - \tau_B \left[1 - e^{-t/\tau_B} \right] \right) . \end{aligned} \quad (2.3.25)$$

We can extract two results from that equation. At short time $t \ll \tau_B$, one has:

$$\begin{aligned} \langle X_t^2 \rangle &\simeq 2 \frac{k_B T}{\gamma} \left(t - \tau_B \left[1 - 1 + \frac{t}{\tau_B} - \frac{t^2}{2\tau_B^2} \right] \right) \\ &= \frac{k_B T}{m} t^2 . \end{aligned} \quad (2.3.26)$$

This is the ballistic regime. If one can experimentally explore times shorter than τ_B one will then measure the real velocity of the particle. At longer times, $t \gg \tau_B$, the MSD is given by:

$$\langle X_t^2 \rangle \simeq 2 \frac{k_B T}{\gamma} t = 2 D t . \quad (2.3.27)$$

This is the diffusive regime where the MSD, as found earlier, Eq.2.3.20 with the over-damped Langevin equation. To study this different results, it can be interesting to simulate the Brownian motion.

2.4 Numerical simulation of bulk Brownian motion

2.4.1 The numerical Langevin Equation

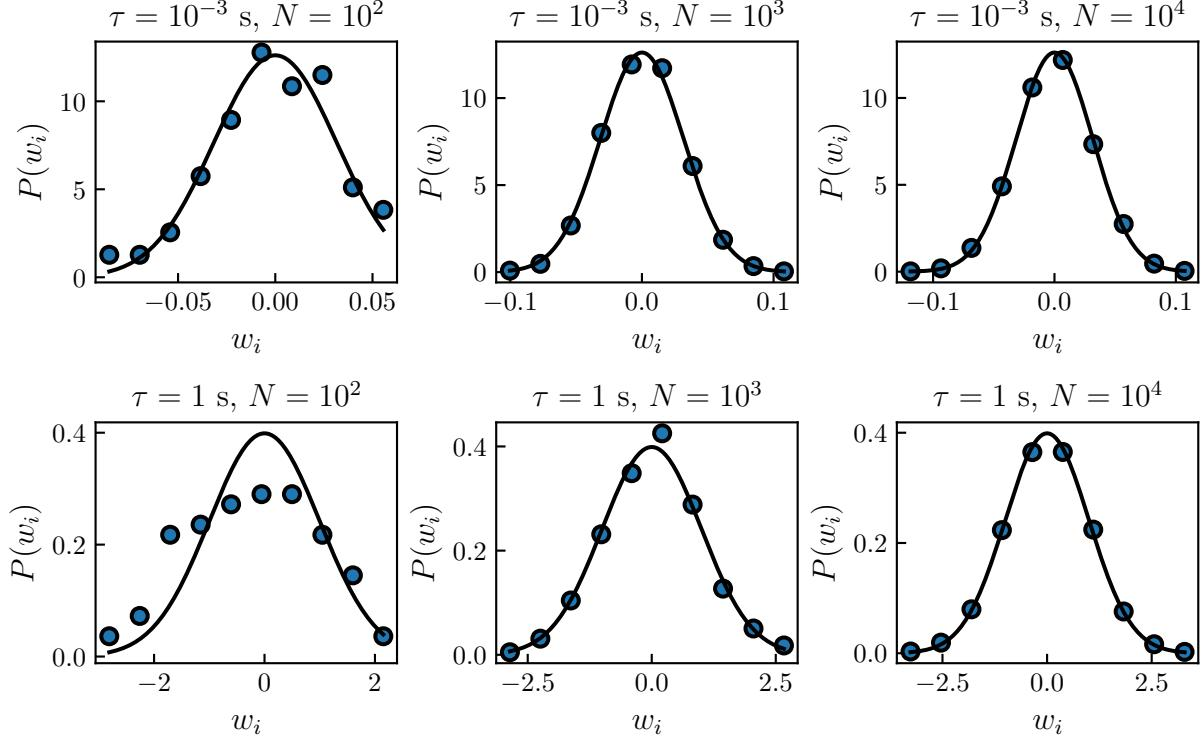


Figure 3: Bullets represents the probability density function of w_i , a Gaussian distributed number with a mean value $\langle w_i \rangle$ and a variance $\langle w_i^2 \rangle = \tau$. The plain black line represents a gaussian of zero mean and a τ variance, Eq.2.4.3. On the first line simulation is done with $\tau = 10^{-3}$ s and $\tau = 1$ s on the second one. Each column correspond to a number of draw N , from the left to the right $N = 10^2$, 10^3 and 10^4 .

The Langevin equation is an ordinary differential equation that can easily be numerically simulated in the bulk case. If one approximate the continuous position of a particle X_t at a time t by a discrete-time sequence x_i which is the solution of the equation at a time $t_i = i\tau$ with τ being the time step of the simulation. One can then use the Euler method to numerically write V_t as

$$V_t \simeq \frac{x_i - x_{i-1}}{\tau} , \quad (2.4.1)$$

and dV_t as

$$\begin{aligned}\frac{dV_t}{dt} &\simeq \frac{\frac{x_i - x_{i-1}}{\tau} - \frac{x_{i-1} - x_{i-2}}{\tau}}{\tau} \\ &= \frac{x_i - 2x_{i-1} + x_{i-2}}{\tau^2}.\end{aligned}\quad (2.4.2)$$

The only term remaining to be computed numerically is the random term dB_t . One can thus replace dB_t/dt by w_i ¹ a Gaussian distributed random number generated with a mean $\langle w_i \rangle = 0$ and a variance $\langle w_i^2 \rangle = \tau$. The Probability Density function (PDF) of the Gaussian distribution is thus given by:

$$P(w_i) = \frac{1}{\sqrt{2\pi\tau}} e^{-\frac{w_i^2}{2\tau}}. \quad (2.4.3)$$

Such a number can be simply generated with the following Python snippet.

```

1 import numpy as np
2
3 tau = 0.5 # time step in seconds
4 wi = np.random.normal(0, np.sqrt(tau))

```

In the latter, `random.normal()` is a built-in Numpy module that permits the generation of Gaussian distributed random numbers. Finally, by combining Eqs.2.4.1, 2.4.2 and w_i , the full Langevin equation becomes:

$$m \frac{x_i - 2x_{i-1} + x_{i-2}}{\tau^2} = -\gamma \frac{x_i - x_{i-1}}{\tau} + \sqrt{2k_B T \gamma} w_i. \quad (2.4.4)$$

From the latter, one can write x_i as:

$$x_i = \frac{2 + \tau/\tau_B}{1 + \tau/\tau_B} x_{i-1} - \frac{1}{1 + \tau/\tau_B} x_{i-2} + \frac{\sqrt{2k_B T \gamma}}{m(1 + \tau/\tau_B)} \tau w_i, \quad (2.4.5)$$

where we can observe that we need two initial condition are needed, the two first positions of the particle. Numerically, those positions could be randomly generated or simply set to 0, if enough statics are generated it will not play much into the results.

¹ The notation w was choose since in mathematical term, a real valued continuous-time stochastic process such as dB_t is called a Wiener process in honor of Norbert Wiener [30].

2.4.2 Simulating Brownian motion using Python

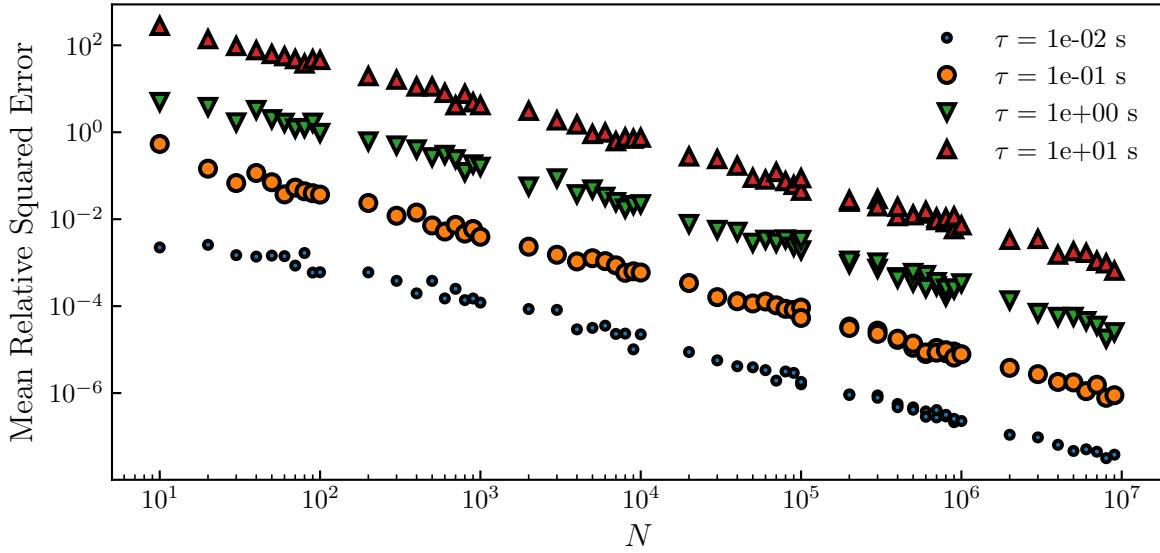


Figure 4: Mean Relative Squared Error (MRSE) of the PDF measured from a generation of N Gaussian random number w_i , and, the actual Gaussian over which the generation is done, Eq.2.4.3. The generation is done over a Gaussian which has a mean value $\langle w_i \rangle = 0$ and the variance $\langle w_i^2 \rangle = \tau$. We explore generation ranging from $N = 10$ to 10^7 and $\tau = 10^{-2}$ to 10 s

Before, deeping into the actual simulation, it could be interresting to ask ourselfe about how long the simulation should be. Indeed, for the different observables' mean value to remain constant we should wait a suffisient amount of time. It is possible to have qualitative approach by generating N number w_i and measuring the resulting PDF $P_c(w_i)$ and looking how much we need to increase N to have $P_c(w_i) \simeq P(w_i)$. As we can see on the Fig.3, for simulation made with $\tau = 10^{-3}$ s and $tau = 1$ s, we obervre that as we increase the number of generated numbers N , the measured PDF, get closer to the real one given by Eq.2.4.3.

To have a more quantitative approach, one can compute the Mean Relative Squared Error (MRSE)) between the measured PDF $P_c(w_i)$ and $P(w_i)$ as a function of the number of generated numbers N , such as:

$$\text{MRSE} = \left\langle \frac{(P_c(w_i) - P(w_i))^2}{P(w_i)^2} \right\rangle_N \quad (2.4.6)$$

where the notation $|_N$ denotes that N numbers are generated. Additionaly, since we measure the $P_c(w_i)$ by doing an histogram, the question of how many bins is used should

be answered. It is possible to use the Freedan-Diaconis rule [31] to compute the width of the bins to be used in a histogram, this rule reads:

$$\text{Bin width} = 2 \frac{\text{IQR}(\{w_i\})}{\sqrt[3]{N}}, \quad (2.4.7)$$

where IQR is the interquartile range, and $\{w_i\}$ a sample of N random numbers. Moreover, one should only take 2 bins as a minimum. The actual number of bins can be computed using the following Python snippet.

```

1 import numpy as np
2
3 def _iqr(wi):
4     """Function to compute interquartile range."""
5     return np.subtract(*np.percentile(x, [75, 25]))
6
7 def optimal_bins(wi):
8     """
9         Function to compute the optimal number of bins using Freedan-diaconis rule.
10        Input: list of random numbers / Output: optimal bins number
11    """
12
13    n = int(diff(wi) / (2 * _iqr(wi) * np.power(len(wi), -1 / 3)))
14
15    if n <= 2:
16        return 2
17    else:
18        return n

```

As we can see on the Fig.4, for τ varying between 10^{-2} and 10 seconds, and, N between 10 and 10^6 , the MRSE decreases as N increases. More over, it is interesting to observe that the MRSE is greater as τ increases for a fix N value. Indeed, as an example we would need to only generate $N = 10^{-3}$ numbers to obtain a MRSE of 10^{-4} for $\tau = 0.1$ s, while we would need to $N = 10^6$ for $\tau = 1$ s.

Now that the Langevin equation is known numerically, one could use it to simulate some Brownian trajectories. A simple way to do the simulation is shown using Python in the Jupyter notebook framework in the appendix.???. A set of trajectory simulated for a fictive particle of radius $a = 1 \mu\text{m}$ and mass $m = 10 \mu\text{g}$ in water is shown in Fig.5-a). For such a particle the diffusive characteristic time is $\tau_B = 0.53\text{s}$. Moreover, as one can see on the Fig.5-b), the MSD is correctly modeled by the Eq.2.3.26 for $\tau \ll \tau_B$ and by the

Eq.2.3.27 for $\tau \gg \tau_B$. Please note that for non-continuous data such as the simulation or experimental trajectories, and for a given time increment Δt , the MSD, is generally defined by:

$$\langle \Delta x^2 \rangle|_t = \langle (x(t + \Delta t) - x(t))^2 \rangle|_t , \quad (2.4.8)$$

where the average $\langle \rangle|_t$ is performed over a time t . Additionally, it can be numerically using the following Python function.

```

1 def msd(x, Dt):
2     """Function that return the MSD for a list of time index Dt for a trajectory x"""
3     _msd = lambda x, t: np.mean((x[:-Dt] - x[Dt:]) ** 2)
4     return [_msd(x, i) for i in t]

```

Additionally, as we have seen earlier, the Langevin Equation can be simplified to it's over-damped version Eq.2.3.10. In this case, the time step of the simulation τ should be greater than the diffusion time τ_B . Thus, one who is interested at the long time statistical properties of the Brownian motion can use the over-damped Langevin equation. In this case by putting $m = 0$ into Eq.2.4.5, one can write x_i as:

$$x_i = x_{i-1} + \sqrt{2D}w_i . \quad (2.4.9)$$

The statistical properties at long time could be retrieved by simulating Brownian motion using the full Langevin equation. But, since the integration scheme used for Eq.2.4.5 requires $\tau \ll \tau_B$ long simulation are necessary to retrieve the over-damped properties. As an example, for the Fig.2 I directly used Eq.2.4.9 for the simulation using the Python Snippet below.

```

1 import numpy as np
2
3 N = 1000 # trajectory length
4 D = 1 # diffusion coefficient
5 tau = 0.5 # time step
6 trajectory = np.cumsum(np.sqrt(2 * D) * np.random.normal(0, np.sqrt(tau), N))

```

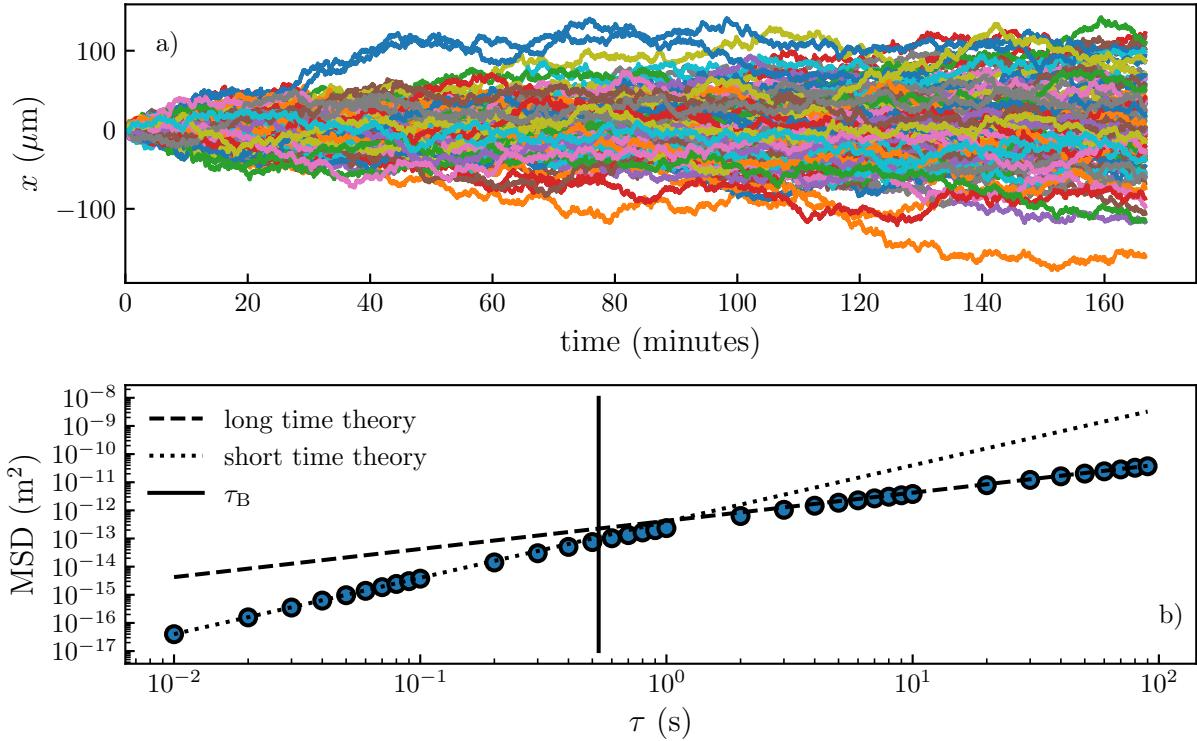


Figure 5: a) Set of 100 trajectories simulated using the full Langevin equation for particle of a radius $a = 1 \mu\text{m}$ and a mass $m = 10 \mu\text{g}$ in water, $\eta = 0.001 \text{ Pa.s}$. The simulations are done with a time step $\tau = 0.01 \text{ s}$. b) Bullets represents the measured Mean Squared Displacement (MSD) of the simulated trajectories. The plain black line represents the characteristic time of the diffusion, here $\tau_B = m/\gamma = 0.53 \text{ s}$. The dotted line represents the MSD theory when $t \ll \tau_B$, $\text{MSD} = \tau^2 k_B T/m$. The dashed line when $t \gg \tau_B$, $\text{MSD} = 2D\tau$. A detailed explanation of the simulation process can be found in the appendix.??.

2.4.3 Speedup using Cython

I would like to point out, that the optimization of a simple simulation of Brownian trajectory can be interesting. Indeed, using a pure Python code as presented in the first part of the appendix.??, the simulation of one trajectory of 10^6 steps, needs 6 s to be computed. Thus, more than 10 minutes should be required to compute the 100 trajectories showed in the Fig.5. This is long due to how Python always verify that what we do is allowed, it thus needs to verify at each step of the `for` loop the object type of each variable. This is in general the main drawback of the interpreted language, one solution is then to compile the part of the code where the `for` loops are computed. One can use the Cython package in order to specify the type of every single variable, once that done, it will convert the lengthy part in C and compile it. As presented in the appendix.??, doing that on full Langevin simulation reduces the time to generate a 10^6 steps trajectory from 6 s to 30 ms thus achieving a speedup of $\simeq 200\times$. Moreover, in the compiled version, we are here speed bound by the random number generation, indeed it takes $24.0 \pm 0.8 \text{ ms}$ using `numpy`.

Additionally, as shown at the end of the appendix.?? even pure C implementation of the random generation can be slower than the `numpy` one, thanks to impressive optimization. Thus, using those tools, this simulation is probably as optimize as it can get.

2.5 Conclusion

In this chapter, we have covered the history of the Brownian motion from the first observation of Robert Brown in the middle of 19th century to it's mathematical and experimental proofs in the early 20s. We have then described mathematically the bulk Brownian motion, and its important stastical properties. Finaly, we have used the later description in order to simulate Brownian motion using the both the full Langevin equation and it's over-damped version. In the following chapter, I will describe experimental methods using light interference properties in order to track colloidal particle.

3 Particle characterization and particle tracking using interference properties

3.1 Introduction

Properties of coherent light to produce interference is widely used in metrology for a long time with, for example, the famous Fabry-Pérot [34, 35] and Michelson interferometers [36]. The latter was initially used to measure earth's rotation and is still used today, in particular, for the recent measurement of gravitational waves [37]. Since the beginning of the century, interest on tracking and characterizing colloidal particles risen thanks to the democratization of micro fluidics and lab-on-a-chip technologies. In the following I will provide some insights on the three most used :

- Reflection Interference Contrast Microscopy (RICM)
- Lorenz-Mie fit
- Rayleigh-Sommerfeld back-propagation

The first one, RICM, uses the principle of optical difference path as a Michelson interferometer. The other two, uses the interference between the light scattered by the colloid and the incident light. Generally, both of the sources are colinear, thus, speak of in-line holography.

3.2 Reflection Interference Contrast Microscopy

Reflection Interference Contrast Microscopy was first introduced in cell biology by Curtis to study embryonic chick heart fibroblast [39] in 1964. RICM gained in popularity 40 years after both in biology and physics [40–45]. It was also used recently in soft matter physics to study elastohydrodynamic lift at a soft wall [38].

When we illuminate a colloid with a plane wave from the bottom, a part of the light is reflected at the surface of the glass substrate and at the colloid's surface. The difference of optical path between two reflection create interference patterns. Let's take an interest at the mathematical description of this phenomenon. In the far field, we can describe two different one-dimensional electric field vectors of the same pulsation ω [46] as:

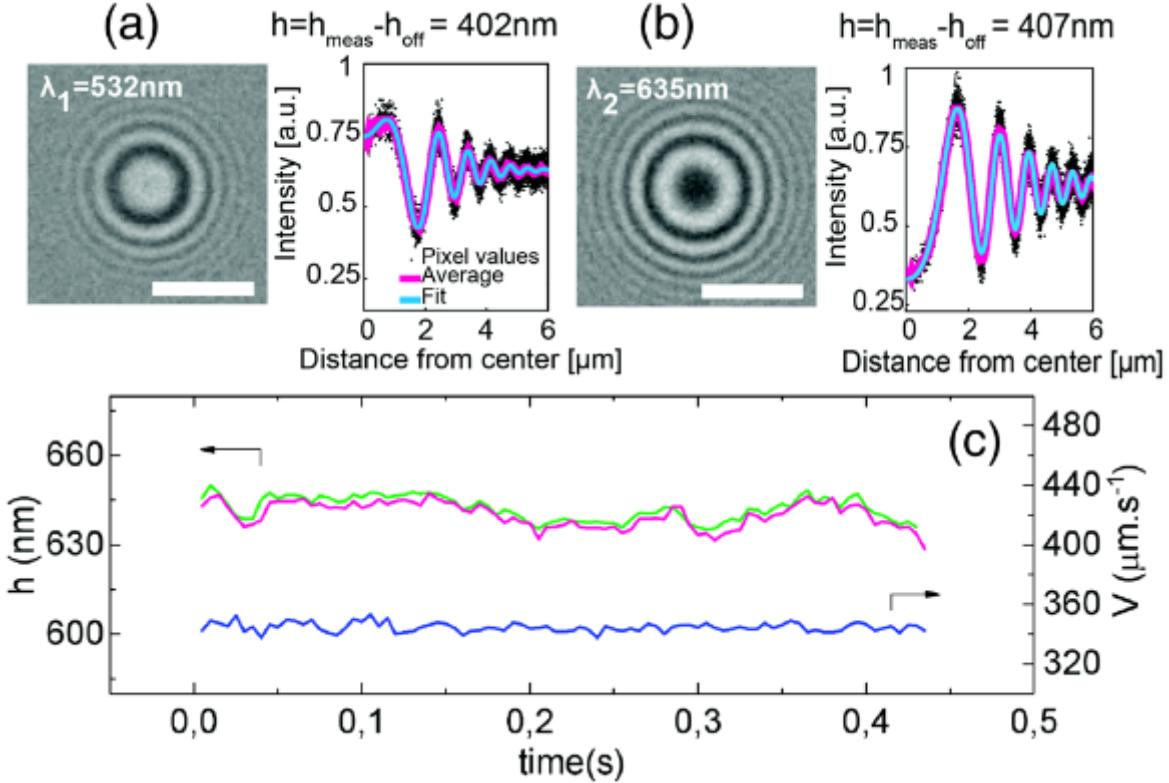


Figure 6: Figure from [38] representing RICM with two wavelengths. (a) Left: interference patterns created with a wavelength $\lambda_1 = 532\text{ nm}$ (scale bar $5\text{ }\mu\text{m}$). Right: radial intensity profile (black dots) extracted from the image, azimuthally averaged (magenta line) and fitted with Eq.3.2.8 to measure the height of the particle (here h). (b) Same as (a) with a wavelength $\lambda_2 = 635\text{ nm}$. (c) Time series of the height of a particle h (green: λ_1 , magenta: λ_2) and the particle velocity measured along the flow in blue.

$$\vec{E}_1(\vec{r}, t) = \vec{E}_{01} \cos(\vec{k}_1 \cdot \vec{r} - \omega t + \epsilon_1) , \quad (3.2.1)$$

and

$$\vec{E}_2(\vec{r}, t) = \vec{E}_{02} \cos(\vec{k}_2 \cdot \vec{r} - \omega t + \epsilon_2) . \quad (3.2.2)$$

Where the k is the wave number $k = 2\pi n_m / \lambda$, λ denoting the illumination wavelength, n_m the optical index of the medium, $\epsilon_{1,2}$ the initial phase of each wave and \vec{r} the position from the source. Here, the origin ($\vec{r} = \vec{0}$) could be taken at the position of the first reflection (on the glass slide) thus at the particle, \vec{r} would be given by the particle's height such that $|r| = z$ the particle-subtract distance. Experimentally, we measure the intensity of the interference patterns, those can be computed from the time averaged squared sum of the electric field $\vec{E} = \vec{E}_1 + \vec{E}_2$. The measured intensity is thus given by:

$$I = \langle \vec{E}^2 \rangle = \langle \vec{E}_1^2 + \vec{E}_2^2 + 2\vec{E}_1 \cdot \vec{E}_2 \rangle = \langle \vec{E}_1^2 \rangle + \langle \vec{E}_2^2 \rangle + 2\langle \vec{E}_1 \cdot \vec{E}_2 \rangle \quad (3.2.3)$$

where $\langle \vec{E}_1^2 \rangle$ and $\langle \vec{E}_2^2 \rangle$ are respectively given by I_1 and I_2 , the incident light intensities. Using the trigonometric formula $2 \cos(a) \cos(b) = \cos(a + b) + \cos(a - b)$ we have:

$$\langle \vec{E}_1 \cdot \vec{E}_2 \rangle = \left\langle \frac{1}{2} \vec{E}_{0_1} \vec{E}_{0_2} \left[\cos(\vec{k}_1 \cdot \vec{r} - \vec{k}_1 \cdot \vec{r} + \phi) + \cos(2\omega t + \phi') \right] \right\rangle. \quad (3.2.4)$$

As we average over the time, the second cos will vanish since in general $\langle \cos(at + b) \rangle_t = 0$ thus:

$$\langle \vec{E}_1 \cdot \vec{E}_2 \rangle = \frac{1}{2} \langle \vec{E}_{0_1} \vec{E}_{0_2} \rangle \cos(\vec{k}_1 \cdot \vec{r} - \vec{k}_2 \cdot \vec{r} + \phi) \quad (3.2.5)$$

with ϕ the phase difference between the two fields, which is generally equal to π due to the reflection properties on a higher index. Indeed, a colloid has generally a greater optical index than the dilution medium. Finally, the total intensity can be read as:

$$I = I_1 + I_2 + 2\sqrt{I_1 I_2} \cos(\vec{k}_1 \cdot \vec{r} - \vec{k}_2 \cdot \vec{r} + \phi) \quad (3.2.6)$$

By taking $k_1 = -k_2$ due to the reflection properties, we have:

$$I = I_1 + I_2 + 2\sqrt{I_1 I_2} \cos\left(\frac{4\pi n_m}{\lambda} z + \phi\right) \quad (3.2.7)$$

If we now suppose that we have a spherical particle at a height z we can develop the radial interference intensity $I(x)$ as [45]:

$$I(x) = A_0 + A_1 e^{-b_1 x^2} + A_2^{-b_2 x^2} \cos\left[\frac{4\pi n_m}{\lambda} (g(x) + z) + \phi\right] \quad (3.2.8)$$

Where A_i and b_i are fit parameters and $g(x)$ denotes the contour of the sphere. Finally, this method is great because the equation is computationally light and permits to have a quick tracking of particles. However, as we can see on Eq.3.2.8, due to the periodicity of the cosinus, the interference pattern will be the same for all heights z separated by a distance $\lambda/2n_m \approx 200$ nm (for $\lambda = 532$ nm and $n_m = 1.33$). It is possible to extend this limitation by using 2 different wavelength to $\approx 1.2 \mu\text{m}$ as used in [38]. Despite the precision of this method which can reach the 10 nm spatial resolution; the measurement ambiguity is not compatible with the study of micro-particle Brownian motion, hence,

RICM is not usable for our context. As a matter of fact, we experimentally reach height span of a few microns.

3.3 Lorenz-Mie Fit

When a colloid is illuminated with a plane wave, a part of the light is scattered. In consequence, the superimposition of the incident field \vec{E}_0 and scattered field \vec{E}_s interferes. The interference patterns thus obtained are called holograms. If the particle size is at the same order of magnitude or greater than the illumination wavelength, it is not possible to use Rayleigh approximations [47]. Indeed, we would need to use what we call the Lorenz-Mie theory which describes the scattering of dielectric spheres; this theory was found by Lorenz and independently by Mie in 1880 and 1908 [48, 49].

It is in the early 2000 that the Lorenz-Mie theory was first used in order to track and characterize particles [50, 51]. Since then, a lot of studies has been realized with this method [52]. In the following I will describe the Lorenz-Mie Fit method. In this part, the height of the particle z is the distance between the particle's center and the focal plane of the objective lens.

Let the incident field be a plane wave uniformly polarized along the axis \hat{e} , with an amplitude E_0 and propagating along the \hat{z} direction :

$$\vec{E}_0(\vec{r}, z) = E_0(\vec{r}) e^{ikz} \hat{e} \quad (3.3.1)$$

Let's consider a particle of radius a at a position \vec{r}_p , the scattered field can be written using the Lorenz-Mie theory [46] as:

$$\vec{E}_s(\vec{r}, z) = \vec{f}_s(k(\vec{r} - \vec{r}_p)) E_0(\vec{r}) \exp(-ikz) \quad (3.3.2)$$

With \vec{f}_s the Lorenz-Mie scattering function [46]. The intensity I that we measure at \vec{r} is given by the superimposition of incident and scattered waves. Since the measurements are done at the focal plane, I is given by:

$$\begin{aligned} I(\vec{r}) &= |\vec{E}_s(\vec{r}, 0) + \vec{E}_0(\vec{r}, 0)|^2 \\ &= E_0^2(\vec{r}) + 2E_0^2 \operatorname{Re} \left(\vec{f}_s(k(\vec{r} - \vec{r}_p)) \hat{e} \right) + |\vec{f}_s(k(\vec{r} - \vec{r}_p))|^2 \end{aligned} \quad (3.3.3)$$

The most of the experimental defects on the images are due to spacial illumination variation caused by dust particle and such. It can be corrected by normalizing the image by the background. In another word, we normalize $I(\vec{r})$ by the intensity of the incident field $I_0 = E_0(\vec{r})^2$ which is the experimental background. It can be measured by different methods, one is to have an empty field of view and the other one, which is more convenient is to take the median of a stack of images. Naturally, for having the latter to work, the movie should be long enough to have the particle diffuse enough, if not a ghost of the particle will appear on the background. This process also permits getting rid of the immobile particle that could generate any additional noise. An example of hologram before and after the normalization is shown in Fig.7 a-c). We write the normalized intensity I/I_0 :

$$\frac{I(\vec{r})}{I_0(\vec{r})} = 1 + 2 \operatorname{Re} \left(\vec{f}_s(k(\vec{r} - \vec{r}_p))\hat{e} \right) + |\vec{f}_s(k(\vec{r} - \vec{r}_p))|^2 \quad (3.3.4)$$

Now that we have the analytical form of the holograms' intensity, it is possible to fit an experimental one to Eq.3.3.4 as shown in Fig.7 d-e). For the sake of completeness, I will detail the Lorenz-Mie scattering function, $\vec{f}_s(k\vec{r})$ which is given by the series:

$$\vec{f}_s(k\vec{r}) = \sum_{n=1}^{n_c} \frac{i^n(2n+1)}{n(n+1)} \left(i a_n \vec{N}_{eln}^{(3)}(k\vec{r}) - b_n \vec{M}_{oln}^{(3)}(k\vec{r}) \right) \quad (3.3.5)$$

where $\vec{N}_{eln}^{(3)}(k\vec{r})$ and $\vec{M}_{oln}^{(3)}(k\vec{r})$ are the vector spherical harmonics. a_n and b_n are some coefficients that depend on the particle and illumination properties. For a spherical and isotropic particle of radius a and refractive index n_p , which is illuminated by a linearly polarized plane wave, the a_n and b_n coefficients are expressed in terms of spherical Bessel j_n and Hankel h_n functions as [46]:

$$a_n = \frac{\zeta^2 j_n(\zeta ka) k a j'_n(ka) - j_n(ka) [\zeta k a j_n(\zeta ka)]'}{\zeta^2 j_n(\zeta ka) k a h_n^{(1)'}(ka) - h_n^{(1)}(ka) \zeta k a j'_n(\zeta ka)} \quad (3.3.6)$$

and

$$b_n = \frac{j_n(\zeta ka) k a j'_n(ka) - j_n(ka) \zeta k a j'_n(mka)}{j_n(\zeta ka) k a h_n^{(1)'}(ka) - h_n^{(1)}(ka) \zeta k a j'_n(mka)}, \quad (3.3.7)$$

where $\zeta = n_p/n_m$ and the prime notation denotes differentiation with respect to the argument. As we can see, the holograms will depends on Eq.3.3.5 and will vary with a lot

of parameters (λ , n_m , n_p , a and \vec{r}_p) which can all be fitted. In general, the illumination wavelength λ and medium index n_m are known and do not need to be fitted. From only one hologram it is thus possible to measure precisely the position of the particle \vec{r}_p and in the same time characterize the radius and optical index of the colloid. As a side note, it is even possible to characterize a particle without a priori knowledge of its characteristics using Bayesian approach [53, 54].

Computing Eq.3.3.5 numerically brings another interesting question, as it is analytically written as a sum over n ; one could ask after which number of terms n_c the series will converge. It has actually been found that the series converge after a number of terms [55]

$$n_c = ka + 4.05(ka)^{1/3} + 2 . \quad (3.3.8)$$

Consequently, larger particles' holograms will need more terms to converge and, hence, are longer to fit. As an example, the largest particles used during my thesis have a radius $a = 2.5 \mu\text{m}$ leading to a number of terms $n_c = 55$ in water and $\lambda = 532 \text{ nm}$, for the smallest ones, where $a = 0.5 \mu\text{m}$ we find $n_c = 18$ which makes a huge difference in practice.

If a reader wants to evaluate an hologram given by the Lorenz-Mie theory for a peculiar particle and position, it can be done in a few lines with the `holopy` module using the following Python snippet which was used to make Fig.13 and 12:

```

1 import holopy as hp
2 from holopy.scattering import calc_holo, Sphere
3
4 sphere = Sphere(n=1.59, r=1.5, center=(4/0.1, 4/0.1, 10))
5 # n is the optical index of the particle, r it's radius in microns
6 # center is its center position in microns.
7
8 medium_index = 1.33
9 illum_wavelen = 0.532
10 illum_polarization = (1, 0)
11 detector = hp.detector_grid(shape=100, spacing=0.1)
12 # shape is the size in pixel of the camera and the spacing is the pixel's size in microns.
13
14 holo = calc_holo(
15     detector, sphere, medium_index, illum_wavelen, illum_polarization, theory="auto"
16 )
17 #the hologram can be directly be plotted using:
18 hp.show(holo)

```

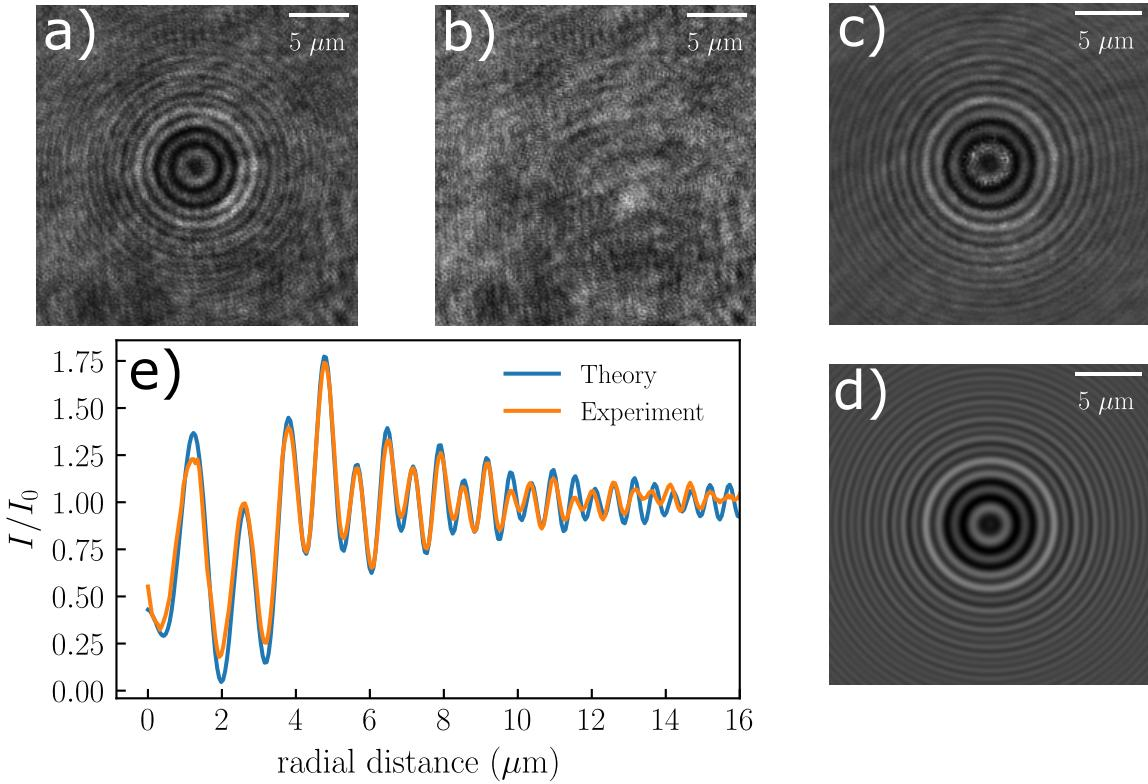


Figure 7: a) Raw hologram of a $2.5 \mu\text{m}$ polystyrene particle measured experimentally with the setup detailed in the chapter 3.5. b) Background obtained by taking the median value of the time series of images of the diffusing particle. c) Normalized hologram given by dividing a) by b). d) Result of the fit of c) using Eq.3.3.4 the particle is found to be at a height $z = 14.77 \mu\text{m}$. e) Comparison of the normalized radial intensity, obtained experimentally from c) and theoretically from d).

3.3.1 Hologram dependence on the particule characteristics

As we can see with the Eq.3.3.5, the in-line holograms vary with the that position, radius and optical index of the particle. For in-line holograms, since the

In order to know what to experimentally expect, one can to compute holograms for particles of different size and height, as shown in the Fig.13 with a fixed optical index $n = 1.59$. In this case, one can observe that as z increases, the hologram's rings gets larger. Unlike a Michelson interferometer or RICM we do not observe the rings scrolling. Additionally, this thickening of the rings can also be observed on the Fig.11, where hologram's intensity profile are plot as a function of the height z . Moreover, we can see that the contrast of the holograms are reduced when the height z is small compared to the radius of the particle. Thus, for having an optimal condition for the fits, one should take care to defocus the enough the objective lens to have $z \gg a$.

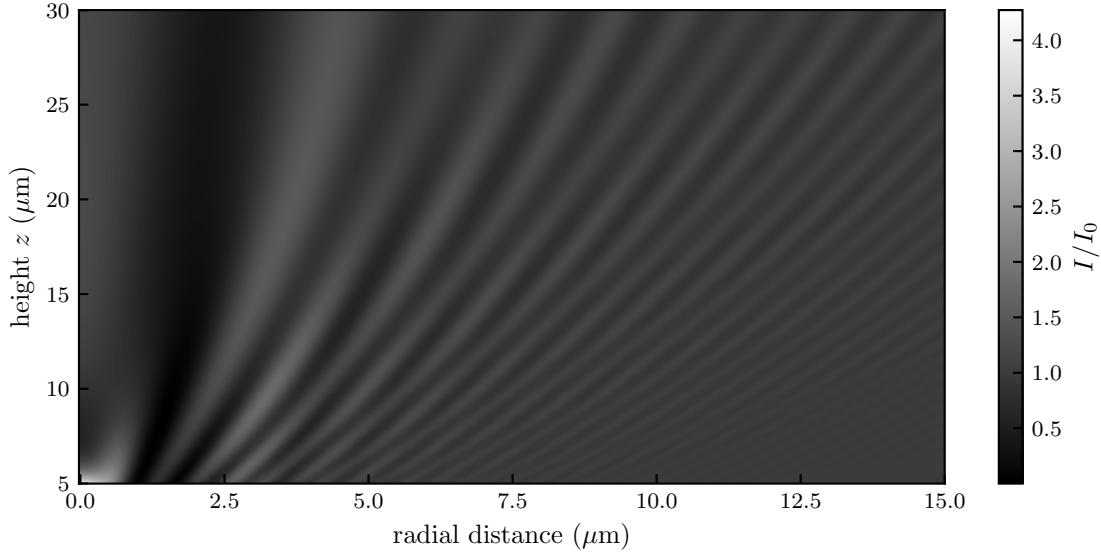


Figure 8: On the left, experimentally measured holograms' radial intensity profile stack, generated from a polystyrene bead of nominal radius $a = 1.5 \pm 0.035 \mu\text{m}$ using the experimental setup explained in chapter 3.5. The calibration of this particle radius and optical index is shown in Fig.17. On the right, the corresponding theoretical stack using the result of each individual hologram's fit.

One can also check how the holograms are varying with the optical index a particle. In the Fig.12, we can observe holograms with a fix height of $z = 15 \mu\text{m}$

Finally, Lorenz-Mie is the most versatile in-line holographic method, indeed, it permits tracking and characterize unique particles even without a priori knowledge. Besides, it is possible to write the Lorenz-Mie function \vec{f}_s for particular cases such as anisotropic [56], non-spherical particles [57] or particle clusters [56, 58] to name a few; such possibilities open the door to a lot of experimental studies. Additionally, it can reach really high precision as the tenth of nanometer on the position and radius as well as 10^{-3} on the optical index [51]. Unfortunately, the Lorenz-Mie fitting suffer from a major drawback which is the time needed to fit one image. For example, a 200 by 200 pixels image, of a $2.5 \mu\text{m}$ particle's hologram, can take up to two minutes to be fitted using a pure and straightforward python algorithm. A lot of work as been done to have faster tracking, such as random-subset fitting [59], GPU (graphical processing unit) acceleration, machine-learning [60, 61] and deep neural networks [62].

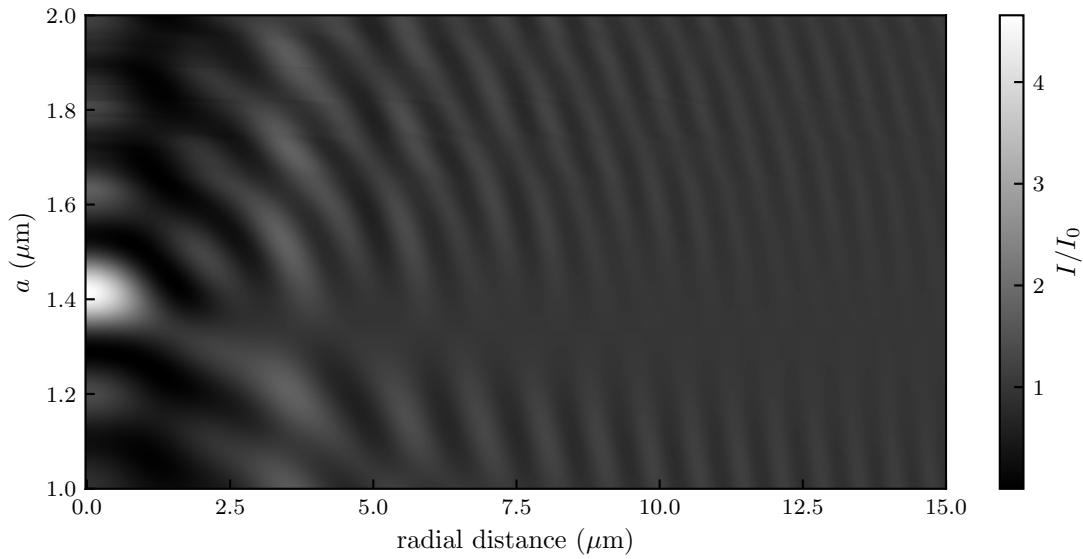


Figure 9: On the left, experimentally measured holograms' radial intensity profile stack, generated from a polystyrene bead of nominal radius $a = 1.5 \pm 0.035 \mu\text{m}$ using the experimental setup explained in chapter 3.5. The calibration of this particle radius and optical index is shown in Fig.17. On the right, the corresponding theoretical stack using the result of each individual hologram's fit.

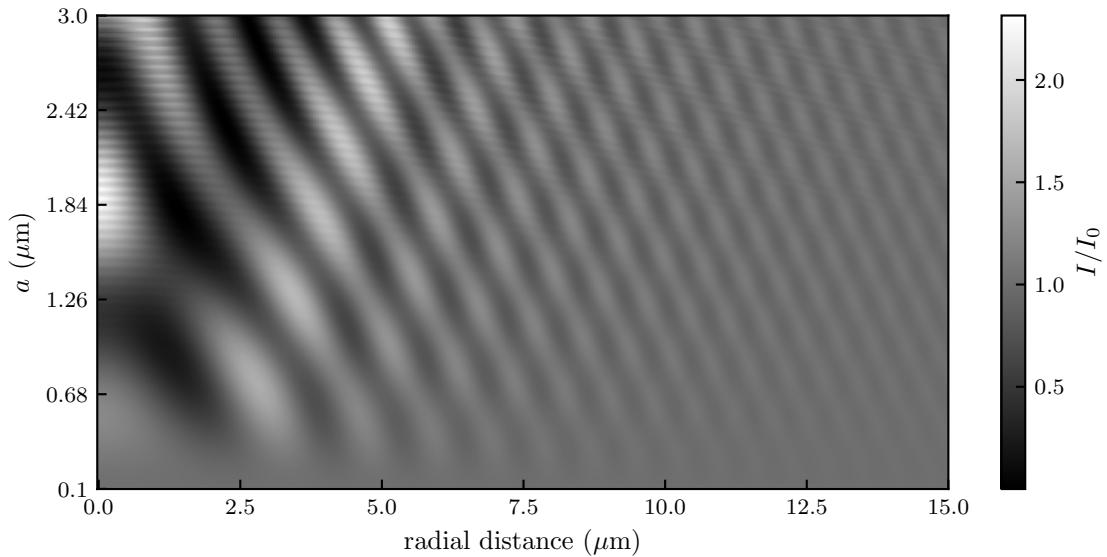


Figure 10: On the left, experimentally measured holograms' radial intensity profile stack, generated from a polystyrene bead of nominal radius $a = 1.5 \pm 0.035 \mu\text{m}$ using the experimental setup explained in chapter 3.5. The calibration of this particle radius and optical index is shown in Fig.17. On the right, the corresponding theoretical stack using the result of each individual hologram's fit.

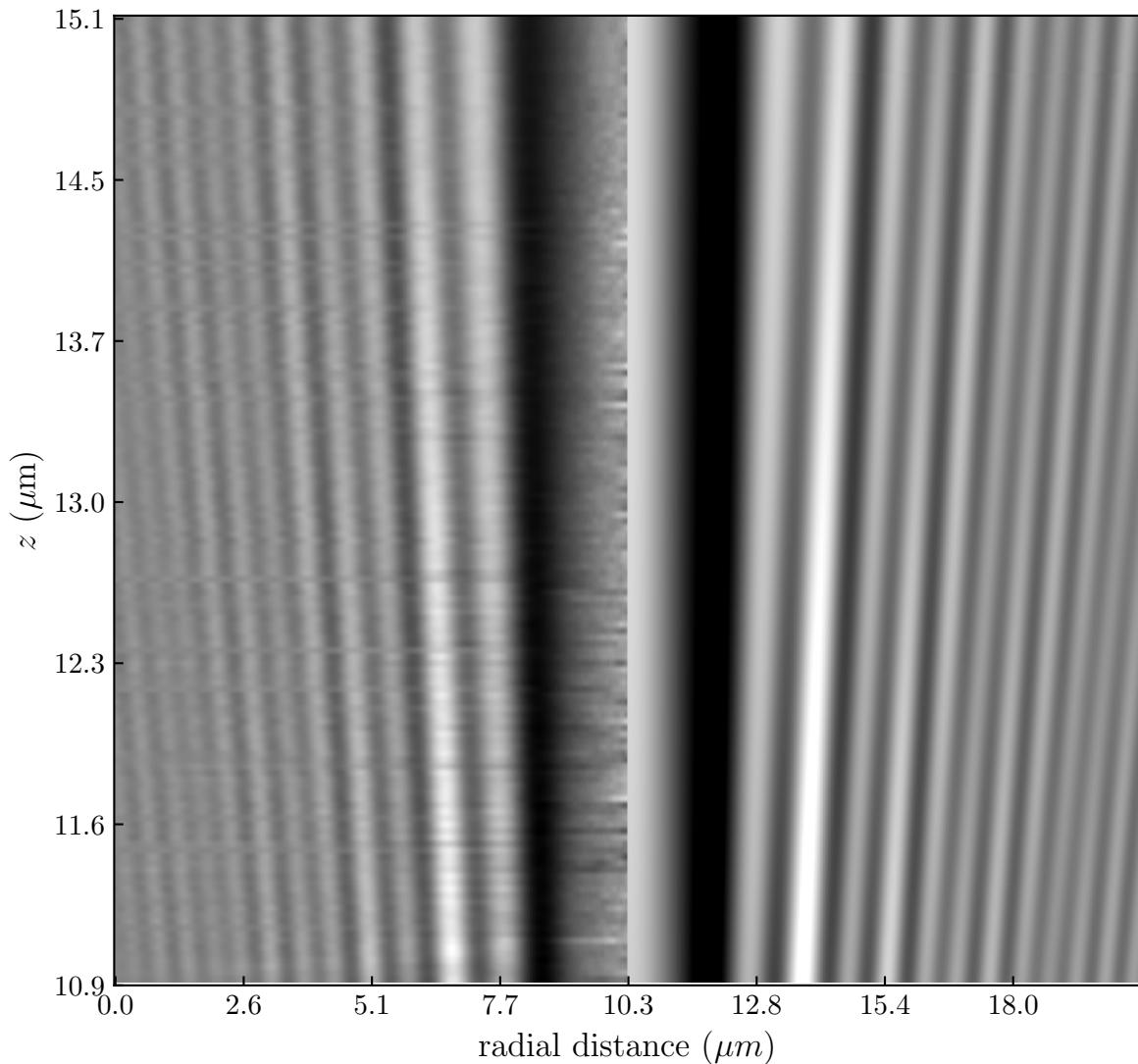


Figure 11: On the left, experimentally measured holograms' radial intensity profile stack, generated from a polystyrene bead of nominal radius $a = 1.5 \pm 0.035 \mu\text{m}$ using the experimental setup explained in chapter 3.5. The calibration of this particle radius and optical index is shown in Fig.17. On the right, the corresponding theoretical stack using the result of each individual hologram's fit.

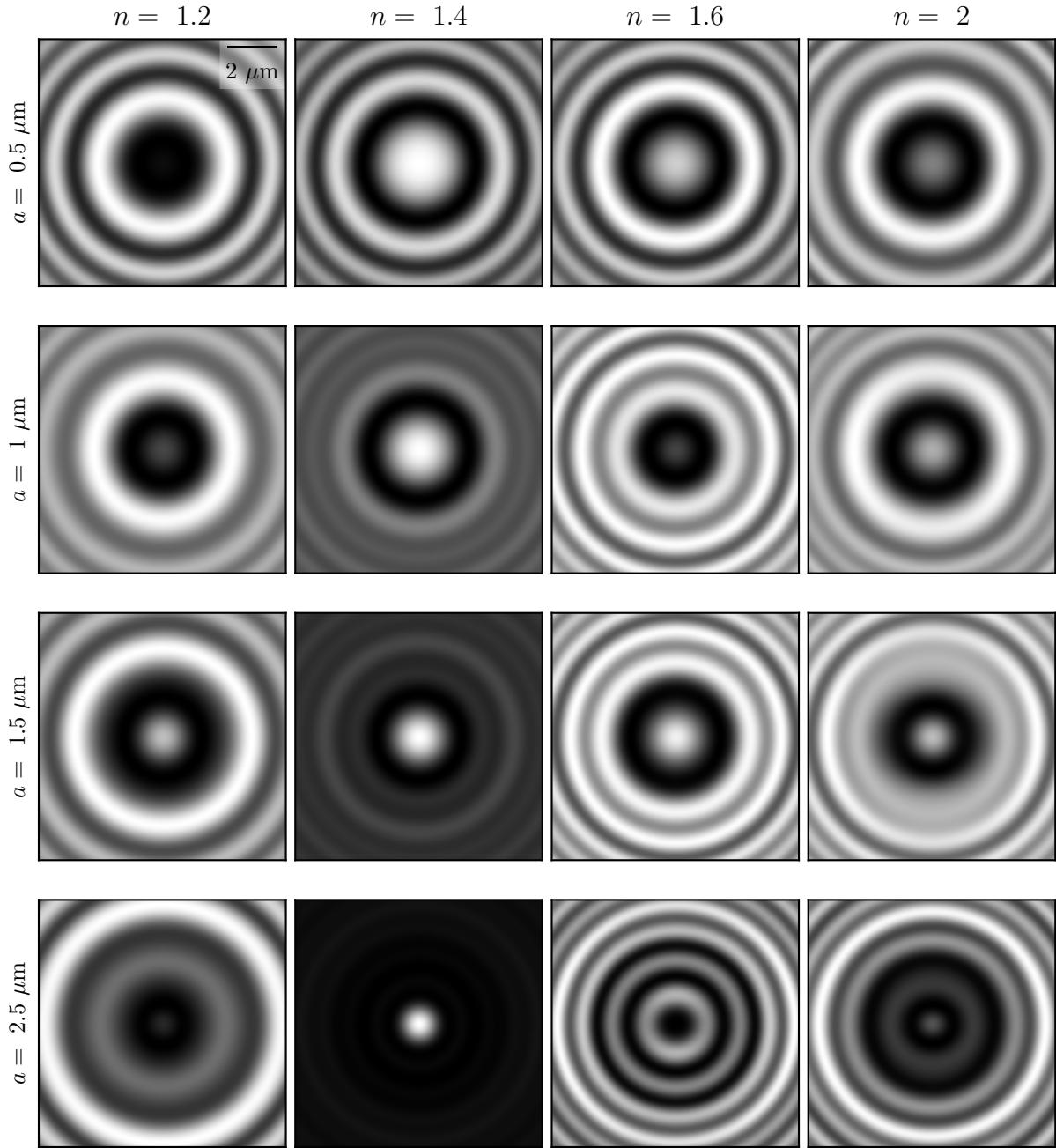


Figure 12: On the left, experimentally measured holograms' radial intensity profile stack, generated from a polystyrene bead of nominal radius $a = 1.5 \pm 0.035 \mu\text{m}$ using the experimental setup explained in chapter 3.5. The calibration of this particle radius and optical index is shown in Fig.17. On the right, the corresponding theoretical stack using the result of each individual hologram's fit.

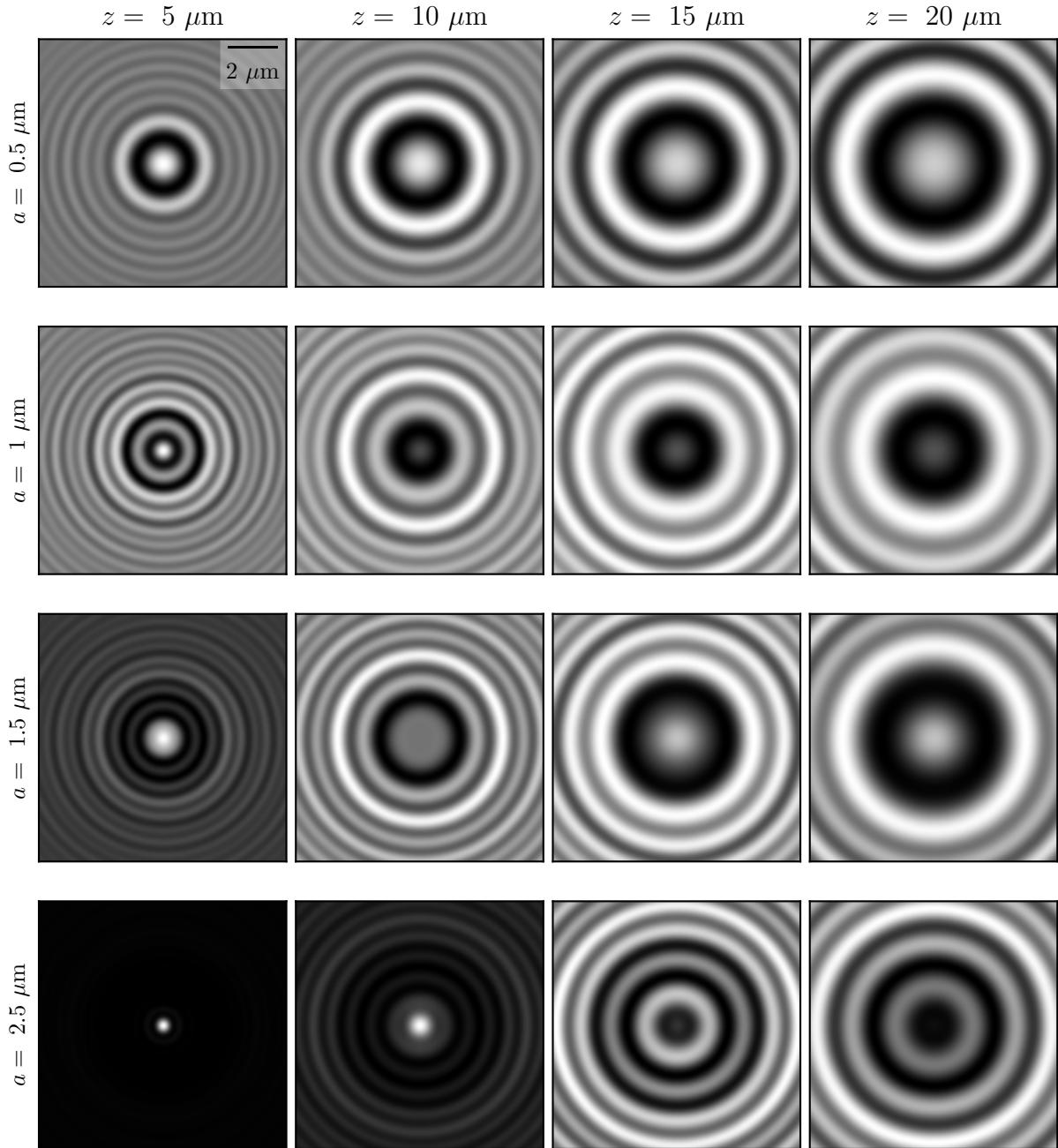


Figure 13: On the left, experimentally measured holograms' radial intensity profile stack, generated from a polystyrene bead of nominal radius $a = 1.5 \pm 0.035 \mu\text{m}$ using the experimental setup explained in chapter 3.5. The calibration of this particle radius and optical index is shown in Fig.17. On the right, the corresponding theoretical stack using the result of each individual hologram's fit.

3.4 Rayleigh-Sommerfeld back-propagation

Rayleigh-Sommerfeld back-propagation [63] works on the same principle as the Lorenz-Mie fitting but assumes that we have small scatterers., such as :

$$|\zeta - 1| \ll 1 \text{ and } ka|\zeta - 1| \ll 1 . \quad (3.4.1)$$

In this case, at the focal plane, the intensity of the scattered field is smaller than the incident field, hence, the term $|\vec{E}_s|^2$ can be ignored. Thus, the normalized intensity, Eq.3.3.4 can be rewritten as:

$$\frac{I(\vec{r})}{I_0(\vec{r})} = 1 + 2 \operatorname{Re} \left(\frac{E_s(\vec{r}, 0)}{E_0(\vec{r})} \right) . \quad (3.4.2)$$

If one can retrieve completely the scattered field from an image, it is possible to reconstruct it above the focal plane by convolution using the Rayleigh-Sommerfeld propagator [64]:

$$h_{-z}(\vec{r}) = \frac{1}{2\pi} \frac{\partial}{\partial z} \frac{e^{ikR}}{R} , \quad (3.4.3)$$

where $R^2 = r^2 + z^2$ and the sign convention on the propagator indicates if the particle is below or above the focal plane. Using this propagator we have:

$$E_s(\vec{r}, z) = E_z(\vec{r}, 0) \otimes h_{-z}(\vec{r}) \quad (3.4.4)$$

By using the convolution theorem [64–67] and supposing a uniform illumination, one can write the reconstructed scattered field at a height z as:

$$E_s(\vec{r}, z) \approx \frac{e^{ikz}}{4\pi^2} \int_{-\infty}^{\infty} B(\vec{q}) H(\vec{q}, -z) e^{i\vec{q}\cdot\vec{r}} d^2 q , \quad (3.4.5)$$

where $B(\vec{q})$ is the Fourier transform of I/I_0 and $H(\vec{q}, -z)$ is given by

$$H(\vec{q}, -z) = e^{iz\sqrt{k^2 - q^2}} . \quad (3.4.6)$$

Finally, using Eq.3.4.5 one can reconstruct the scattered field and intensity since $I(\vec{r}) = |E_s(\vec{r})|^2$ as shown in Fig.14. Moreover, by finding the position where the field is the brightest as shown in red the Fig.14, we measure the position of the particle. Those equations are way less computational intensive than the Lorenz-Mie function Eq.3.3.5. Thus tracking can be way faster, moreover, Fourier transforms can be largely accelerated using GPU. Additionally, as the propagator Eq.3.4.3 take only into account the intensity of the image, this method does not require any information on the particle and number of particles. As a matter of fact, to write Eq.3.4.5 one just need to assume that we have spherical colloids. Thus, this method is great to reconstruct the 3D position of a lot of particles or clusters formations. However, the major drawback is that it is the less precise of the presented measurements and that we can't use it to characterize the particles generating the holograms.

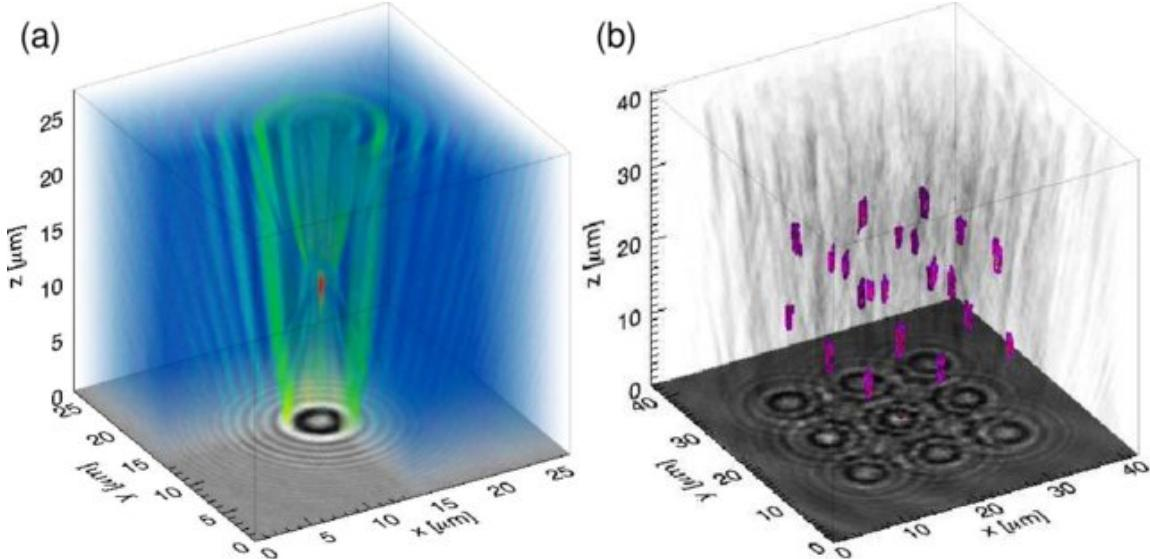


Figure 14: Figure from [65] a) Volumetric reconstruction using Eq.3.4.5 of the scattered intensity of single colloidal sphere, colored by intensity. b) Volumetric reconstructions of 22 individual $1.58 \mu\text{m}$ diameter silica spheres organized in bcc lattice using holographic optical tweezers in distilled water. Colored regions indicate the isosurface of the brightest 1 percent of reconstructed voxels.

3.4.1 Conclusion

Finally, the method we choose is the Lorenz-Mie fitting method, since this it permits the characterization of single particles. Indeed, since we are interested to fine effects near the surface, we need to know perfectly the radius of the particle we have recorded. This feature also make our all process calibration free, as we don't need to assume any physical properties. In the following, the experimental setup is going to be detailed.

3.5 Experimental setup

In order to observe the holograms we use an homemade inverted microscope as shown on the Fig.15 and shematized in Fig.16. A sample consists of a parallelepipedic chamber ($1.5\text{ cm} \times 1.5\text{ cm} \times 150\text{ }\mu\text{m}$), made from two glass covers, a parafilm spacer, and sealed with vacuum grease, containing a dilute suspension of spherical polystyrene beads. We used 3 different sizes, of nominal radii $0.56\text{ }\mu\text{m}$, $1.5\text{ }\mu\text{m}$ and $2.5\text{ }\mu\text{m}$, at room temperature T , in distilled water (type 1, MilliQ device) of viscosity $\eta = 1\text{ mPa.s}$. The sample is illuminated by a collimated laser beam with a $521\text{ }\mu\text{m}$ wavelength. As depicted in the chapter 3.3, the light scattered by one colloidal particle at a given time t interferes with the incident beam. An oil-immersion objective lens (x60 magnification, 1.30 numerical aperture) collects the resulting instantaneous interference pattern, and relays it to a camera (Basler acA1920-155um) with a 51.6 nm/pixel resolution (see Fig.7a)). The exposure time of the camera is set to $\tau_{\text{expo}} = 3\text{ ms}$ to avoid motion-induced blurring of the image, as a general rule, the particle should not diffuse more than the pixel size during that time such that here $2D\tau_{\text{expo}} < 51.6\text{ nm}$.

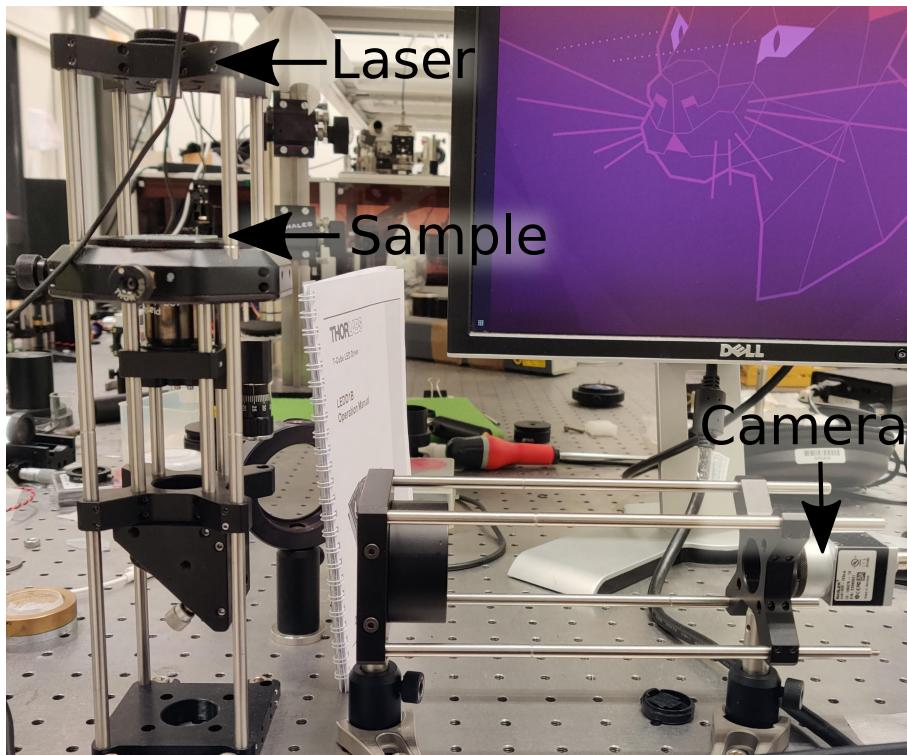


Figure 15: Photo of the custom build microscope used along my thesis. It is mainly composed of Thorlabs cage system. The camera used is a Basler acA1920-155um, we use a x60 magnification and 1.30 numerical aperture oil-immersion objective lens. The light source is a collimated $521\text{ }\mu\text{m}$ wavelength laser.

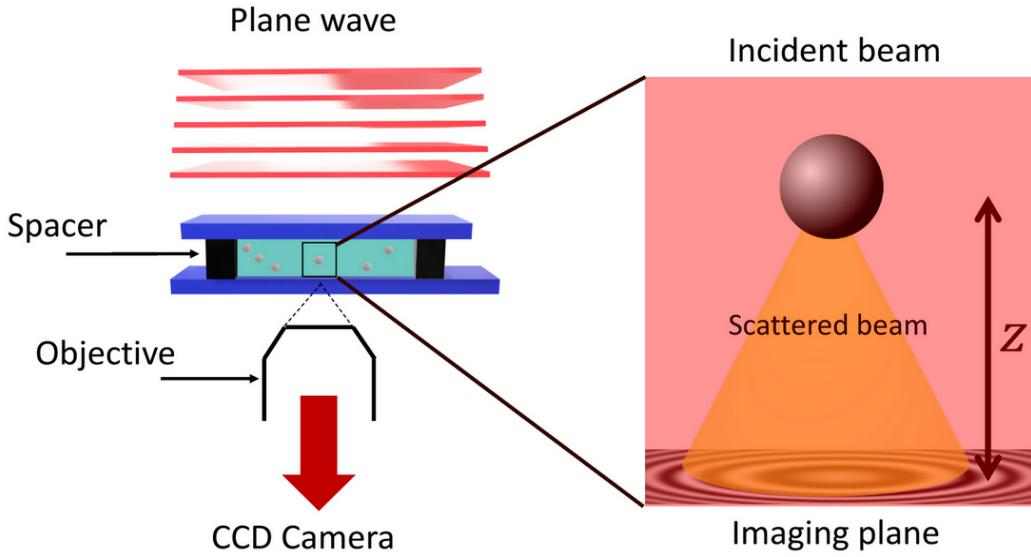


Figure 16: Schematic of the experimental setup. A laser plane wave of intensity I_0 illuminates the chamber containing a dilute suspension of micro-spheres in water. The light scattered by a particle interferes with the incident beam onto the focal plane of an objective lens, that magnifies the interference pattern and relays it to a camera.

3.6 Hologram fitting strategy

3.6.1 How to fasten the process ?

As presented in the section 3.3 about the Lorenz-Mie fitting, the main drawback is the time to fit an image, from 30 seconds for the images of 100×100 pixels to a few minutes for the 500×500 pixels. We can directly see a bottleneck, indeed, if we want to track one trajectory made of 100 000 images we would need to wait a minimum of ≈ 70 days; for a series of images that need only a few minutes to be shot experimentaly. When I started my PhD, two groups, the Grier's lab and the Manoharan's lab, had already introduced python packages, respectively, Pylorenzmie and Holopy in order to inverse holograms. They had introduced ways to only fit a set of randomly chosen pixels, and demonstrated that taking only 1% of the image pixels, could lead to similar precision and improve considerably the fit's execution time [59]. Unfortunately, even if this is faster, it leads to a few images per second and still is too long for the amount of data we wanted to have. Ironically, this part of my project is certainly the one where I spent the most my time, and I actually learned a lot of things on code optimization and computer cluster usage. It's around the half of my thesis, that Pylorenzmie got a new commit on their github repository which was telling that they succeeded on using GPU acceleration using

CUDA. This was not an easy task since they needed to reconstruct the Bessel functions in an understandable way for the GPU, fortunately it is possible to do so by using continued fractions [55]. This humongous update permits fitting whole images at a whooping speed improvement of 20 fps. At this speed, we fit the tridimension position of the particle, the radius and optical index. To have a more reliable and fast tracking, what we do is that we fit with all free parameters the first 10 000 images of a movie. We then determine the physical properties of the colloidal particle and then fit the whole movie with only the position as a free parameter.

3.6.2 Radius and optical index characterization

Once the data of the radius and optical index retrieved, the quantity we can look at is the distribution of measurements. Using 10 000 measurements we can plot the histograms of the measured a and n_p .

This simple histogram could suffice to measure the physical properties of the colloidal particle. However, we can go a bit further and look at the 2D histogram of the a and n_p as presented in the fig.17 here smoothed using a Gaussian kernel density estimator. As we can see it is not isotropic, and it seems that the measurement of n_p and a are correlated.

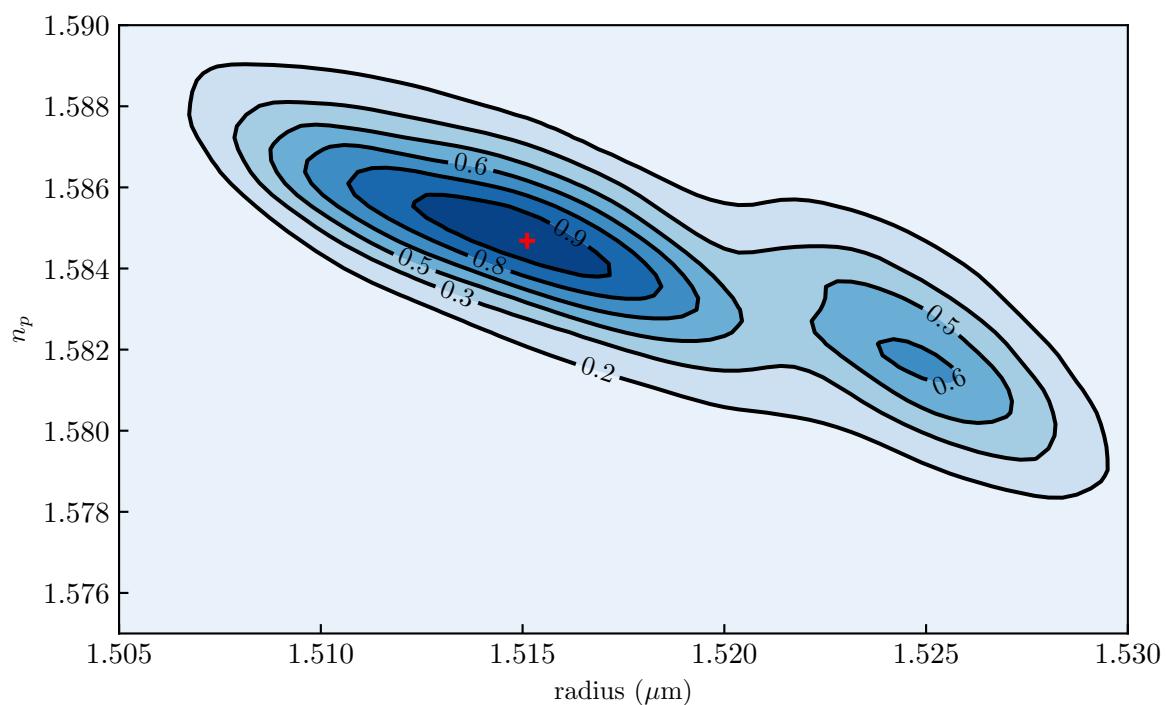


Figure 17: 2D Probability density function of the measurements of the optical index n_p and radius a . Black lines indicate iso-probability. Taking the 10% top probability, we measure $n_p = 1.585 \pm 0.002$ and $a = 1.514 \pm 0.003 \mu\text{m}$.

4 infer

4.1 The confined Brownian motion

We have seen that the bulk Brownian motion is well known and documented for a long time. But, in the real world, the boundaries are not at infinity and could play a role in the process of diffusion. Indeed, it was theorized by H. Faxen [32] that the presence of a wall would change the Stokes-Einstein relation with a viscosity dependent to the position of the particle. As the particle get closer to a surface, the presence of the non-slip boundary condition make the fluid harder to push, thus increasing the local viscosity of the particle. This variation of the viscosity will be different for orthogonal and parallel displacement to the wall, thus we write respectively η_{\perp} and η_{\parallel} with η_0 being the fluid viscosity and z the height of the particle:

$$\eta_{\perp} = \frac{4}{3}\eta_0 \sinh \beta \sum_{n=1}^{\infty} \frac{n(n+1)}{2n-12n+3} \left[\frac{2\sinh(2n+1)\beta + (2n+1)\sinh 2\beta}{4\sinh^2(n+1/2)\beta - (2n+1)^2\sinh^2\beta} - 1 \right], \quad (4.1.1)$$

and

$$\eta_{\parallel} = \eta_0 \left[1 - \frac{9}{16}\xi + \frac{1}{8}\xi^3 - \frac{45}{256}\xi^4 - \frac{1}{16}\xi^5 \right]^{-1}, \quad (4.1.2)$$

where $\xi = \frac{a}{z+a}$ and $\beta = \cosh^{-1}(\xi)$. It is possible to simplify the form of η_{\perp} by using a Padé approximation, which is correct up to 1% of accuracy:

$$\eta_{\perp} = \eta_0 \frac{6z^2 + 9az + 2a^2}{6z^2 + 2az}. \quad (4.1.3)$$

Of course, this local viscosity is directly reflected on the diffusive properties of the particle, hence a local diffusion coefficient, which we write:

$$D_i(z) = \frac{k_B T}{6\pi\eta_i(z)a}. \quad (4.1.4)$$

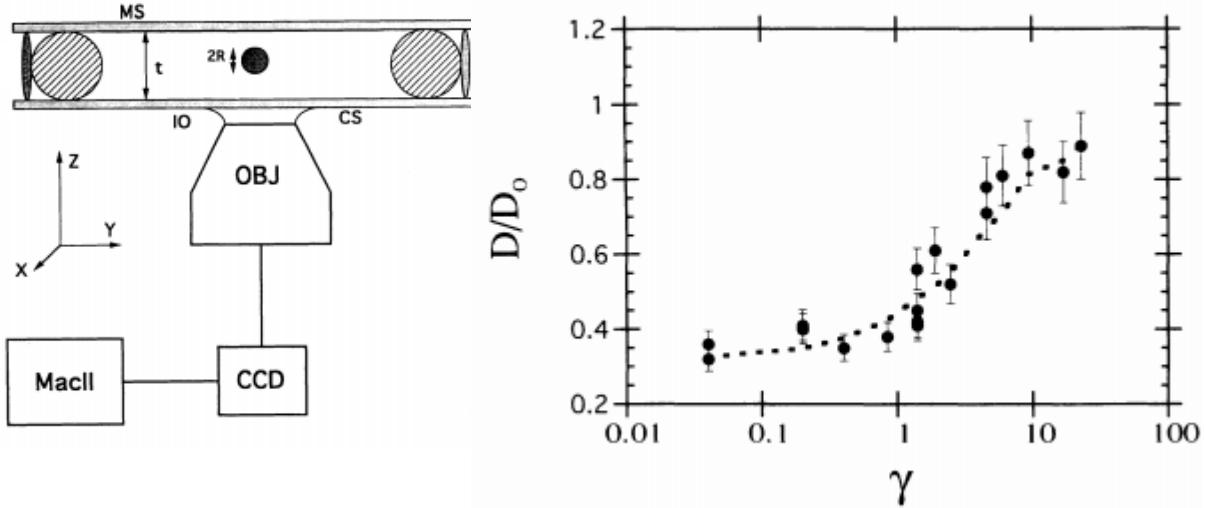


Figure 18: Figure extracted from [13], on the left is the experimental setup used. It is an inverted microscope used in order to track particle of size $2R$ inside a cell of thickness t . On the right is their final result, where they measure the diffusion parallel coefficient D_{\perp} given by Eq.4.1.1.2, here normalized by D_0 the bulk diffusion coefficient as a function of γ a confinement constant $\gamma = (\langle z \rangle - a)/a$.

One of the first experimental measurement of the local diffusion coefficient was brought by Faucheuix and Libchaber [13] where they measured the mean diffusion coefficient with various gaps and particle radius their results can be found in the Fig.18.

Another interesting physical aspect to take into account when looking at confined Brownian motion is the potential the particle is lying into. Let's first consider the weight of the particle. Indeed, if the particle density does not match the fluid' one, a spherical particle will lie in a gravity potential given by:

$$U_g(z) = \frac{4}{3}\pi a^3(\rho_p - \rho_f)gz , \quad (4.1.5)$$

that we can rewrite for simplicity

$$\frac{U_g(z)}{k_B T} = \frac{z}{\ell_B} , \quad (4.1.6)$$

with ℓ_B the Boltzmann length which represents the balance between the kinetic energy and the weight of the particle:

$$\ell_B = \frac{k_B T}{\frac{4}{3}\pi a^3 \Delta \rho g} . \quad (4.1.7)$$

Let's now consider the interactions with the substrate, glass slides when immersed in water do charge negatively as well as polystyrene particles that we use. We will then have repulsive electrostatic interactions between the wall and the particles, the corresponding potential can be written as [33]:

$$\frac{U_{\text{elec}}(z)}{k_B T} = B e^{-z/\ell_D} , \quad (4.1.8)$$

where B is the amplitude of electrostatic interactions, representing the surface charges and ℓ_D being the Debye length, which is the characteristic length of the electrostatic interactions. The particle is thus lying in a total potential given by:

$$\frac{U(z)}{k_B T} = B e^{-z/\ell_D} + \frac{z}{\ell_B} . \quad (4.1.9)$$

From this total potential one can construct the Gibbs-Boltzmann distribution in position:

$$P_{\text{eq}}(z) = A e^{\frac{U}{k_B T}} , \quad (4.1.10)$$

where A is a normalization constant so that $\int P_{\text{eq}} = 1$. This distribution gives us the probability to find the particle at a height z . The exponential decay due to the gravity was first measured by Perrin [5] by methodically counting through a microscope the number of colloids in suspension as a function on the height.

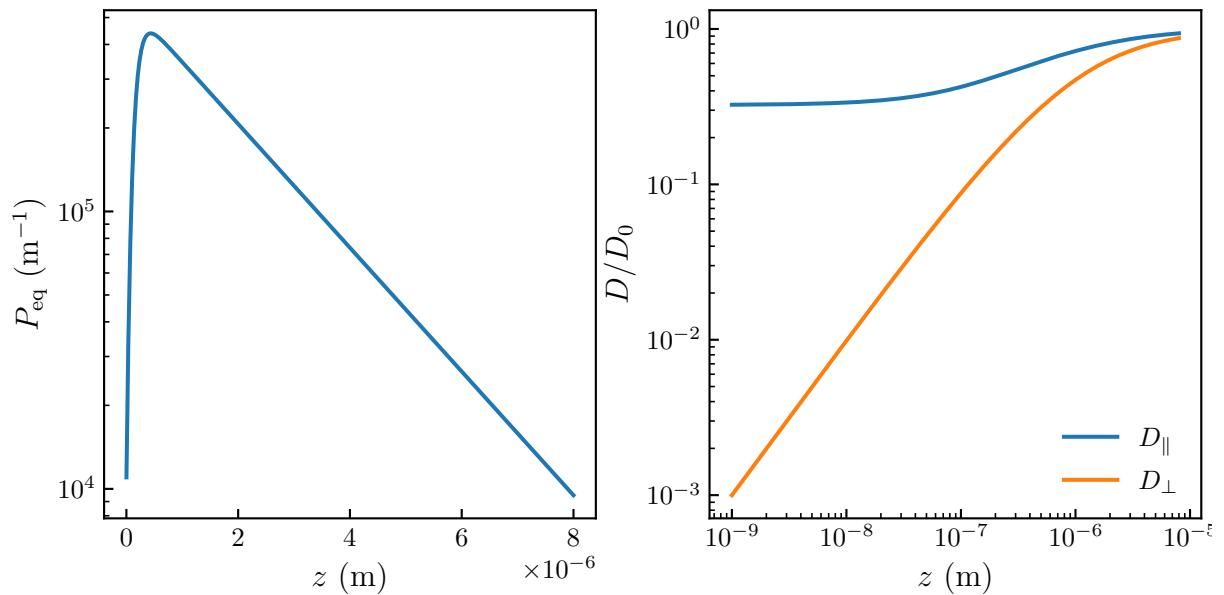


Figure 19: On the left, plot of the Gibbs-Boltzmann distribution Eq.4.1.10 for $a = 1 \mu\text{m}$, $B = 4$, $\ell_D = 100 \text{ nm}$ and $\Delta\rho = 50 \text{ kg.m}^{-3}$. On the right, local diffusion coefficient normalized by bulk diffusion coefficient $D_0 = k_B T/\gamma$, given by Eq.4.1.2 and Eq.4.1.1

References

- [1] R. Baraniuk, D. Donoho, and M. Gavish, “The science of deep learning”, Proceedings of the National Academy of Sciences **117**, Publisher: National Academy of Sciences Section: Introduction, 30029–30032 (2020).
- [2] B. Lemieux, A. Aharoni, and M. Schena, “Overview of DNA chip technology”, Molecular Breeding **4**, 277–289 (1998).
- [3] Á. Ríos, M. Zougagh, and M. Avila, “Miniaturization through lab-on-a-chip: utopia or reality for routine laboratories? a review”, Analytica Chimica Acta **740**, 1–11 (2012).
- [4] A. Einstein, “Über die von der molekularkinetischen Theorie der Wärme geforderte Bewegung von in ruhenden Flüssigkeiten suspendierten Teilchen”, Annalen der Physik **vol. 4, t. 17** (1905).
- [5] J. Perrin, *Les Atomes*, Google-Books-ID: A0ltBQAAQBAJ (CNRS Editions, Nov. 14, 2014), 199 pp.
- [6] B. U. Felderhof, “Effect of the wall on the velocity autocorrelation function and long-time tail of brownian motion †”, The Journal of Physical Chemistry B **109**, 21406–21412 (2005).
- [7] M. V. Chubynsky and G. W. Slater, “Diffusing diffusivity: a model for anomalous, yet brownian, diffusion”, Physical Review Letters **113**, 098302 (2014).
- [8] A. V. Chechkin, F. Seno, R. Metzler, and I. M. Sokolov, “Brownian yet non-gaussian diffusion: from superstatistics to subordination of diffusing diffusivities”, Physical Review X **7**, 021002 (2017).
- [9] C. I. Bouzigues, P. Tabeling, and L. Bocquet, “Nanofluidics in the debye layer at hydrophilic and hydrophobic surfaces”, Physical Review Letters **101**, Publisher: American Physical Society, 114503 (2008).
- [10] L. Joly, C. Ybert, and L. Bocquet, “Probing the nanohydrodynamics at liquid-solid interfaces using thermal motion”, Physical Review Letters **96**, Publisher: American Physical Society, 046101 (2006).
- [11] J. Mo, A. Simha, and M. G. Raizen, “Brownian motion as a new probe of wettability”, The Journal of Chemical Physics **146**, Publisher: American Institute of Physics, 134707 (2017).

- [12] E. R. Dufresne, T. M. Squires, M. P. Brenner, and D. G. Grier, “Hydrodynamic coupling of two brownian spheres to a planar surface”, *Physical Review Letters* **85**, Publisher: American Physical Society, 3317–3320 (2000).
- [13] L. P. Faucheux and A. J. Libchaber, “Confined brownian motion”, *Physical Review E* **49**, 5158–5163 (1994).
- [14] E. R. Dufresne, D. Altman, and D. G. Grier, “Brownian dynamics of a sphere between parallel walls”, *EPL (Europhysics Letters)* **53**, Publisher: IOP Publishing, 264 (2001).
- [15] H. B. Eral, J. M. Oh, D. v. d. Ende, F. Mugele, and M. H. G. Duits, “Anisotropic and hindered diffusion of colloidal particles in a closed cylinder”, *Langmuir* **26**, Publisher: American Chemical Society, 16722–16729 (2010).
- [16] P. Sharma, S. Ghosh, and S. Bhattacharya, “A high-precision study of hindered diffusion near a wall”, *Applied Physics Letters* **97**, Publisher: American Institute of Physics, 104101 (2010).
- [17] J. Mo, A. Simha, and M. G. Raizen, “Broadband boundary effects on brownian motion”, *Physical Review E* **92**, 062106 (2015).
- [18] M. Matse, M. V. Chubynsky, and J. Bechhoefer, “Test of the diffusing-diffusivity mechanism using near-wall colloidal dynamics”, *Physical Review E* **96**, 042604 (2017).
- [19] D. C. Prieve, “Measurement of colloidal forces with TIRM”, *Advances in Colloid and Interface Science* **82**, 93–125 (1999).
- [20] A. Banerjee and K. Kihm, “Experimental verification of near-wall hindered diffusion for the brownian motion of nanoparticles using evanescent wave microscopy”, *Physical review. E, Statistical, nonlinear, and soft matter physics* **72**, 042101 (2005).
- [21] S. Sainis, V. Germain, and E. Dufresne, “Statistics of particle trajectories at short time intervals reveal fN-scale colloidal forces”, *Physical review letters* **99**, 018303 (2007).
- [22] G. Volpe, L. Helden, T. Brettschneider, J. Wehr, and C. Bechinger, “Influence of noise on force measurements”, *Physical Review Letters* **104**, 170602 (2010).
- [23] M. Li, O. Sentissi, S. Azzini, G. Schnoering, A. Canaguier-Durand, and C. Genet, “Subfemtonewton force fields measured with ergodic brownian ensembles”, *Physical Review A* **100**, 063816 (2019).

- [24] S. K. Sainis, V. Germain, and E. R. Dufresne, “Statistics of particle trajectories at short time intervals reveal fN-scale colloidal forces”, *Physical Review Letters* **99**, 018303 (2007).
- [25] B. Robert, “XXVII. a brief account of microscopical observations made in the months of june, july and august 1827, on the particles contained in the pollen of plants; and on the general existence of active molecules in organic and inorganic bodies”, *The Philosophical Magazine* **4**, Taylor & Francis, 161–173 (1828).
- [26] S. Peter, “Brownian motion”, **Brownian motion**.
- [27] J. Perrin, “Mouvement brownien et molécules”, *J. Phys. Theor. Appl.* **9**, 5–39 (1910).
- [28] A. Genthon, “The concept of velocity in the history of brownian motion”, *The European Physical Journal H* **45**, 49–105 (2020).
- [29] P. Langevin, “Sur la théorie du mouvement brownien”, *C. R. Acad. Sci. (Paris)* **146**, 530–533 **65**, 1079–1081 (1908).
- [30] R. Durrett, *Probability: theory and examples*, 5th ed., Cambridge Series in Statistical and Probabilistic Mathematics (Cambridge University Press, Cambridge, 2019).
- [31] D. Freedman and P. Diaconis, “On the histogram as a density estimator:l 2 theory”, *Zeitschrift fur Wahrscheinlichkeitstheorie und Verwandte Gebiete* **57**, 453–476 (1981).
- [32] H. Faxen, “Fredholm integral equations of hydrodynamics of liquids i”, *Ark. Mat., Astron. Fys* **18**, 29–32 (1924).
- [33] J. N. Israelachvili, *Intermolecular and surface forces*, Google-Books-ID: MVbWB-hubrgIC (Academic Press, May 29, 2015), 706 pp.
- [34] C. Fabry and A. Pérot, “Théorie et application d’une nouvelle méthode de spectroscopie interferentielle.”, *Ann. Chim. Phys.*, **7** (1899).
- [35] A. Perot and C. Fabry, “On the application of interference phenomena to the solution of various problems of spectroscopy and metrology”, *The Astrophysical Journal* **9**, 87 (1899).
- [36] A. A. Michelson and E. W. Morley, “On the relative motion of the earth and the luminiferous ether”, *American Journal of Science* **s3-34**, Publisher: American Journal of Science Section: Extraterrestrial geology, 333–345 (1887).

- [37] LIGO Scientific Collaboration and Virgo Collaboration et al., “GW151226: observation of gravitational waves from a 22-solar-mass binary black hole coalescence”, Physical Review Letters **116**, in collab. with B. P. Abbott, Publisher: American Physical Society, 241103 (2016).
- [38] H. S. Davies, D. Débarre, N. El Amri, C. Verdier, R. P. Richter, and L. Bureau, “Elastohydrodynamic lift at a soft wall”, Physical Review Letters **120**, 198001 (2018).
- [39] A. S. Curtis, “THE MECHANISM OF ADHESION OF CELLS TO GLASS. a STUDY BY INTERFERENCE REFLECTION MICROSCOPY”, The Journal of Cell Biology **20**, 199–215 (1964).
- [40] T. J. Filler and E. T. Peuker, “Reflection contrast microscopy (RCM): a forgotten technique?”, The Journal of Pathology **190**, 635–638 (2000).
- [41] P. A. Siver and J. Hinsch, “THE USE OF INTERFERENCE REFLECTION CONTRAST IN THE EXAMINATION OF DIATOM VALVES”, Journal of Phycology **36**, 616–620 (2000).
- [42] I. Weber, “[2] reflection interference contrast microscopy”, in *Methods in enzymology*, Vol. 361, Biophotonics, Part B (Academic Press, Jan. 1, 2003), pp. 34–47.
- [43] L. Limozin and K. Sengupta, “Quantitative reflection interference contrast microscopy (RICM) in soft matter and cell adhesion”, Chemphyschem: A European Journal of Chemical Physics and Physical Chemistry **10**, 2752–2768 (2009).
- [44] F. Nadal, A. Dazzi, F. Argoul, and B. Pouliquen, “Probing the confined dynamics of a spherical colloid close to a surface by combined optical trapping and reflection interference contrast microscopy”, Applied Physics Letters **79**, 3887–3889 (2002).
- [45] J. Raedler and E. Sackmann, “On the measurement of weak repulsive and frictional colloidal forces by reflection interference contrast microscopy”, Langmuir **8**, 848–853 (1992).
- [46] C. F. Bohren and D. R. Huffman, *Absorption and scattering of light by small particles* (Wiley, Apr. 1998).
- [47] H. J. W. Strutt, “LVIII. on the scattering of light by small particles”, The London, Edinburgh, and Dublin Philosophical Magazine and Journal of Science **41**, Publisher: Taylor & Francis _eprint: <https://doi.org/10.1080/14786447108640507>, 447–454 (1871).

- [48] L. Lorenz, *Lysbevægelsen i og uden for en af plane Lysbølger belyst Kugle*, Google-Books-ID: hnE7QwAACAAJ (1890), 62 pp.
- [49] G. Mie, “Beiträge zur optik trüber medien, speziell kolloidaler metallösungen”, *Analnen der Physik* **330**, eprint: <https://onlinelibrary.wiley.com/doi/pdf/10.1002/andp.19083300302> 377–445 (1908).
- [50] B. Ovryn and S. H. Izen, “Imaging of transparent spheres through a planar interface using a high-numerical-aperture optical microscope”, *JOSA A* **17**, Publisher: Optical Society of America, 1202–1213 (2000).
- [51] S.-H. Lee, Y. Roichman, G.-R. Yi, S.-H. Kim, S.-M. Yang, A. v. Blaaderen, P. v. Oostrum, and D. G. Grier, “Characterizing and tracking single colloidal particles with video holographic microscopy”, *Optics Express* **15**, Publisher: Optical Society of America, 18275–18282 (2007).
- [52] J. Katz and J. Sheng, “Applications of holography in fluid mechanics and particle dynamics”, *Annual Review of Fluid Mechanics* **42**, eprint: <https://doi.org/10.1146/annurev-fluid-121108-145508>, 531–555 (2010).
- [53] P. Gregory, *Bayesian logical data analysis for the physical sciences: a comparative approach with mathematica® support*, Google-Books-ID: idkLAQAAQBAJ (Cambridge University Press, Apr. 14, 2005), 496 pp.
- [54] T. G. Dimiduk and V. N. Manoharan, “Bayesian approach to analyzing holograms of colloidal particles”, *Optics Express* **24**, Publisher: Optical Society of America, 24045–24060 (2016).
- [55] W. J. Lentz, “Generating bessel functions in mie scattering calculations using continued fractions”, *Applied Optics* **15**, Publisher: Optical Society of America, 668–671 (1976).
- [56] J. Fung and V. N. Manoharan, “Holographic measurements of anisotropic three-dimensional diffusion of colloidal clusters”, *Physical Review E* **88**, 020302 (2013).
- [57] A. Wang, T. G. Dimiduk, J. Fung, S. Razavi, I. Kretzschmar, K. Chaudhary, and V. N. Manoharan, “Using the discrete dipole approximation and holographic microscopy to measure rotational dynamics of non-spherical colloidal particles”, *Journal of Quantitative Spectroscopy and Radiative Transfer* **146**, 499–509 (2014).

- [58] R. W. Perry, G. Meng, T. G. Dimiduk, J. Fung, and V. N. Manoharan, “Real-space studies of the structure and dynamics of self-assembled colloidal clusters”, *Faraday Discussions* **159**, Publisher: The Royal Society of Chemistry, 211–234 (2013).
- [59] T. G. Dimiduk, R. W. Perry, J. Fung, and V. N. Manoharan, “Random-subset fitting of digital holograms for fast three-dimensional particle tracking”, *Applied Optics* **53**, G177 (2014).
- [60] A. Yevick, M. Hannel, and D. G. Grier, “Machine-learning approach to holographic particle characterization”, *Optics Express* **22**, 26884 (2014).
- [61] M. D. Hannel, A. Abdulali, M. O’Brien, and D. G. Grier, “Machine-learning techniques for fast and accurate feature localization in holograms of colloidal particles”, *Optics Express* **26**, Publisher: Optical Society of America, 15221–15231 (2018).
- [62] L. E. Altman and D. G. Grier, “CATCH: characterizing and tracking colloids holographically using deep neural networks”, *The Journal of Physical Chemistry B* **124**, Publisher: American Chemical Society, 1602–1610 (2020).
- [63] L. Wilson and R. Zhang, “3d localization of weak scatterers in digital holographic microscopy using rayleigh-sommerfeld back-propagation”, *Optics Express* **20**, 16735 (2012).
- [64] J. W. Goodman, *Introduction to fourier optics*, Google-Books-ID: ow5xs_Rtt9AC (Roberts and Company Publishers, 2005), 520 pp.
- [65] F. C. Cheong, B. J. Krishnatreya, and D. G. Grier, “Strategies for three-dimensional particle tracking with holographic video microscopy”, *Optics Express* **18**, Publisher: Optical Society of America, 13563–13573 (2010).
- [66] G. C. Sherman, “Application of the convolution theorem to rayleigh’s integral formulas”, *JOSA* **57**, Publisher: Optical Society of America, 546–547 (1967).
- [67] U. Schnars and W. P. Jüptner, “Digital recording and reconstruction of holograms in hologram interferometry and shearography”, *Applied Optics* **33**, 4373–4377 (1994).